

Fast Diffusion Sampler for Inverse Problems by Geometric Decomposition

Hyungjin Chung
KAIST

hj.chung@kaist.ac.kr

Suhyeon Lee
KAIST

suhyeon.lee@kaist.ac.kr

Jong Chul Ye
KAIST

jong.ye@kaist.ac.kr

Abstract

Diffusion models have shown exceptional performance in solving inverse problems. However, one major limitation is the slow inference time. While faster diffusion samplers have been developed for unconditional sampling, there has been limited research on conditional sampling in the context of inverse problems. In this study, we propose a novel and efficient diffusion sampling strategy that employs the geometric decomposition of diffusion sampling. Specifically, we discover that the samples generated from diffusion models can be decomposed into two orthogonal components: a “denoised” component obtained by projecting the sample onto the clean data manifold, and a “noise” component that induces a transition to the next lower-level noisy manifold with the addition of stochastic noise. Furthermore, we prove that, under some conditions on the clean data manifold, the conjugate gradient update for imposing conditioning from the denoised signal belongs to the clean manifold, resulting in a much faster and more accurate diffusion sampling. Our method is applicable regardless of the parameterization and setting (i.e., VE, VP). Notably, we achieve state-of-the-art reconstruction quality on challenging real-world medical inverse imaging problems, including multi-coil MRI reconstruction and 3D CT reconstruction. Moreover, our proposed method achieves more than 80 times faster inference time than the previous state-of-the-art method.

1. Introduction

Diffusion models [12, 34] are the state-of-the-art generative model that learns to generate data by gradual denoising, starting as a sample from the reference distribution (e.g. Gaussian). In addition to superior sample quality in the unconditional sampling of the data distribution, it was shown that one can use unconditional diffusion models as *generative priors* that model the data distribution [7, 18], and incorporate the information from the forward physics model along with the measurement \mathbf{y} to sample from the posterior distribution $p(\mathbf{x}|\mathbf{y})$. This property is especially intriguing when seen in the context of Bayesian inference, as we can separate the parameterized prior $p_\theta(\mathbf{x})$ from the

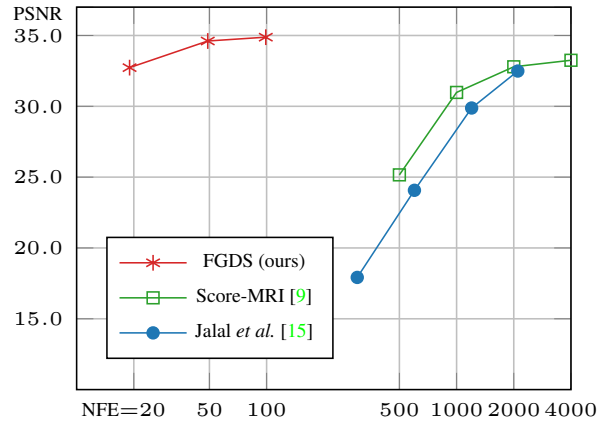


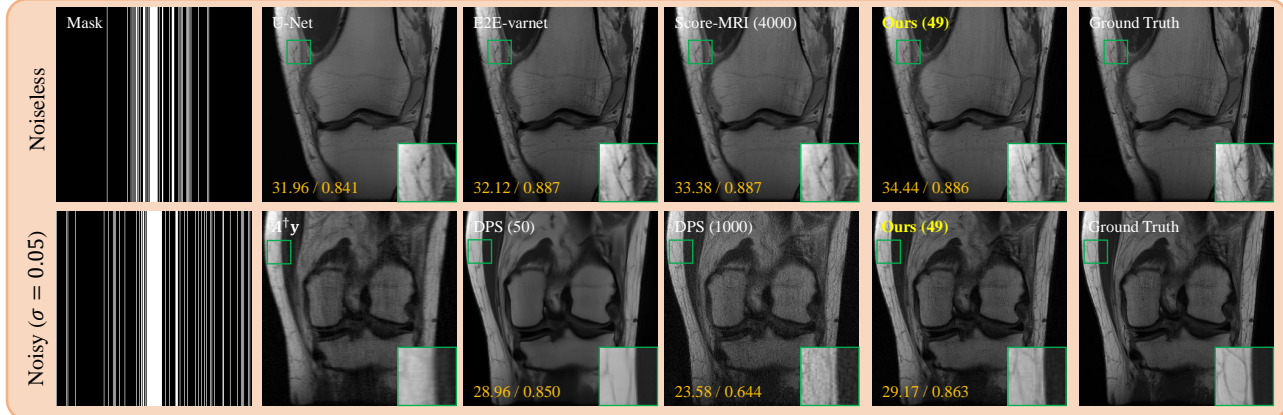
Figure 1: Parallel imaging MR reconstruction evaluation PSNR vs. NFE (log scale). Reconstruction from 1D uniform random $\times 4$ acceleration [39].

measurement model (i.e. likelihood) $p(\mathbf{y}|\mathbf{x})$ to construct the posterior $p_\theta(\mathbf{x}|\mathbf{y}) \propto p_\theta(\mathbf{x})p(\mathbf{y}|\mathbf{x})$. In another word, one can use the same model *regardless* of the forward model at hand. Throughout the manuscript, we refer to this class of methods as **D**iffusion model-based **I**nverse problem **S**olvers (DIS).

For inverse problems in medical imaging, e.g. magnetic resonance imaging (MRI), computed tomography (CT), it is often required to accelerate the measurement process by subsampling the measurements¹. However, the design of sampling patterns may vary vastly according to the circumstances (e.g. vendor, sequence, etc.) and hence it is important for the reconstruction algorithm to be adaptable to different possibilities. Supervised learning schemes show weakness on this aspect as they overfit to the measurement types that were used during training. On the other hand, it is easy to see that diffusion models will be particularly strong in this aspect as they are agnostic to the different forward models (i.e. sub-sampling patterns) at inference. Indeed, it was shown in some of the pioneering works that diffusion-based reconstruction algorithms have high generalizability [15, 9, 33, 6].

¹One can view both sparse-view CT (SV-CT) and limited angle CT (LA-CT) problems as sub-sampling in the Radon measurement space.

(a) Multi-coil CS-MRI



(b) 3D Sparse-view CT

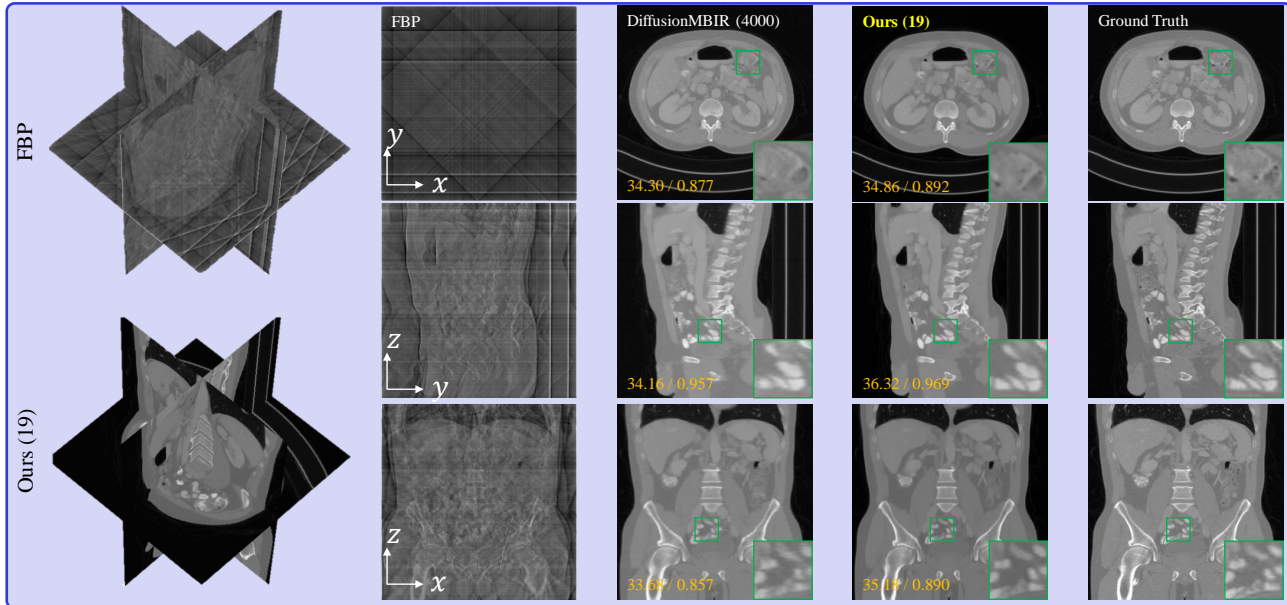


Figure 2: Representative reconstruction results. (a) Multi-coil MRI reconstruction, (b) 3D sparse-view CT. Numbers in parenthesis: NFE.

While showing superiority in performance and generalization capacity, slow inference time is known to be a critical drawback of diffusion models. Over the years, significant efforts have been made toward alleviating this downside by 1) devising a better ODE/SDE solver [17, 23, 22], 2) leveraging a recursive distillation approach [28, 25], etc. Nevertheless, most works are focused on *unconditional* sampling, leaving the conditional sampling acceleration rather under-explored. Some recent works [24, 38] have aimed specifically for *guided* diffusion sampling. Specifically, Lu *et al.* [24] targeted classifier-free guidance [13] (CFG), the de facto standard for text-to-image (T2I) guidance, while Wizardowns *et al.* [38] aimed for gradient guidance [10, 7], subsuming classifier guidance [34]. However, even the works that devise faster conditional diffusion methods focus extensively on T2I guidance, which is inherently different from DIS. See appendix C for the discussion.

On the other hand, one of the most widely acknowledged accelerated diffusion sampling strategies is the denoising diffusion implicit model (DDIM) [30], where the stochastic ancestral sampling of denoising diffusion probabilistic models (DDPM) can be transitioned to deterministic sampling, and thereby accelerate the sampling. Accordingly, DDIM sampling has been well incorporated in solving low-level vision inverse problems [18, 31]. In a recent application of DDIM for linear image restoration tasks, the authors proposed an algorithm dubbed denoising diffusion null-space models (DDNM) [37] where one step null-space modification is made to impose consistency. However, the sampling strategy has not been shown to be successful in practical medical imaging contexts, when the forward model is significantly more complex (e.g. parallel imaging (PI) CS-MRI, 3D modalities). Furthermore, it is unclear how the algorithm is related to the existing literature of conditional sampling

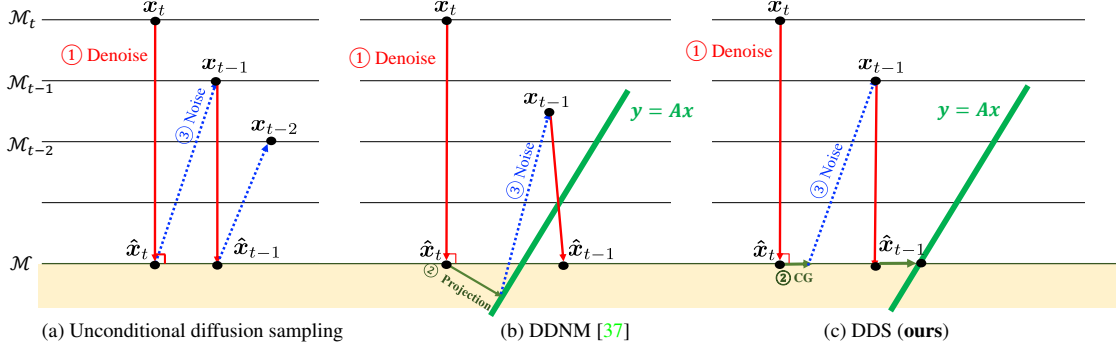


Figure 3: Geometry of diffusion samplers. The orthogonality of $\hat{\mathbf{x}}_t$ is up to a scale factor for VP and exact for VE.

approaches that take into account the geometry of the manifold [7, 5]

To address this issue, we conduct a thorough analysis of the geometry of diffusion sampling under the assumption that the clean data manifold is a lower-dimensional subspace, specifically a Krylov subspace [21], which has been commonly employed in inverse problems. Our analysis reveals that the generated samples can be decomposed into two orthogonal components: 1) A “denoised” component obtained by projecting the sample onto the clean data manifold, and 2) A “noise” component that is orthogonal to the clean data manifold and induces a transition to the next lower-level noisy manifold with the addition of stochastic noise. We also show that conjugate gradient (CG) updates, initiated from the denoised image, remain on the clean manifold. Our analysis holds for both variance-preserving (VP) and variance-exploding (VE) sampling schemes.

Taking inspiration from this geometric insight, we present a comprehensive conditional diffusion sampling approach. Our proposal involves utilizing CG-based optimization for condition guidance, which is solely applied to the denoised component. Subsequently, we add the noise component, ensuring that the generated samples shifts to the next level of the noisy manifold. Our proposed method enhances the previous diffusion model-based methods in two primary ways:

1. We improve the sampling strategy by ensuring that it conforms to the geometry of diffusion, which is suitable for both VE/VP diffusion;
2. We implement a CG-based conditioning strategy that ensures the sample in the intermediate steps to say on the clean manifold, leading to improved accuracy.

The combined strategy, dubbed **Decomposed Diffusion Sampling (DDS)**, yields *better* performance with much-reduced sampling time (20~50 NFE, $\times 80 \sim 200$ acceleration; See Fig. 1 for comparison, Fig. 2 for representative results), and is shown to be applicable to a variety of challenging inverse problem tasks: multi-coil MRI recon-

struction and 3D CT reconstruction (sparse view, limited angle).

2. Background

Diffusion models Diffusion models [12] attempt to model the data distribution $p_{\text{data}}(\mathbf{x})$ by constructing a hierarchical latent variable model

$$p_{\theta}(\mathbf{x}_0) = \int p_{\theta}(\mathbf{x}_T) \prod_{t=1}^T p_{\theta}^{(t)}(\mathbf{x}_{t-1}|\mathbf{x}_t), \quad (1)$$

where $\mathbf{x}_{\{1, \dots, T\}} \in \mathbb{R}^d$ are *noisy* latent variables that have the same dimension as the data random vector $\mathbf{x}_0 \in \mathbb{R}^d$, defined by the Markovian forward conditional densities

$$q(\mathbf{x}_t|\mathbf{x}_{t-1}) = \mathcal{N}(\mathbf{x}_t|\beta_t\mathbf{x}_{t-1}, (1 - \beta_t)I), \quad (2)$$

$$q(\mathbf{x}_t|\mathbf{x}_0) = \mathcal{N}(\mathbf{x}_t|\sqrt{\bar{\alpha}_t}\mathbf{x}_0, (1 - \sqrt{\bar{\alpha}_t})I). \quad (3)$$

Here, the noise schedule β_t is an increasing sequence of t , with $\bar{\alpha}_t := \prod_{i=1}^t \alpha_i$, $\alpha_t := 1 - \beta_t$. Training of diffusion models amount to training a multi-noise level residual denoiser (i.e. epsilon matching)

$$\min_{\theta} \mathbb{E}_{\mathbf{x}_t \sim q(\mathbf{x}_t|\mathbf{x}_0), \mathbf{x}_0 \sim p_{\text{data}}(\mathbf{x}_0), \epsilon \sim \mathcal{N}(0, I)} \left[\|\epsilon_{\theta}^{(t)}(\mathbf{x}_t) - \epsilon\|_2^2 \right],$$

such that $\epsilon_{\theta^*}^{(t)}(\mathbf{x}_t) \simeq \frac{\mathbf{x}_t - \sqrt{\bar{\alpha}_t}\mathbf{x}_0}{\sqrt{1 - \bar{\alpha}_t}}$. Furthermore, it can be shown that epsilon matching is equivalent to the denoising score matching (DSM) [14, 32] objective up to a constant with different parameterization

$$\min_{\theta} \mathbb{E}_{\mathbf{x}_t, \mathbf{x}_0, \epsilon} \left[\|\mathbf{s}_{\theta}^{(t)}(\mathbf{x}_t) - \nabla_{\mathbf{x}_t} \log q(\mathbf{x}_t|\mathbf{x}_0)\|_2^2 \right], \quad (4)$$

such that $\mathbf{s}_{\theta^*}^{(t)}(\mathbf{x}_t) \simeq -\frac{\mathbf{x}_t - \sqrt{\bar{\alpha}_t}\mathbf{x}_0}{1 - \bar{\alpha}_t} = -\epsilon_{\theta^*}^{(t)}(\mathbf{x}_t)/\sqrt{1 - \bar{\alpha}_t}$. For notational simplicity, we often denote $\hat{\mathbf{s}}_t, \hat{\epsilon}_t, \hat{\mathbf{x}}_t$ instead of $\mathbf{s}_{\theta^*}^{(t)}(\mathbf{x}_t), \epsilon_{\theta^*}^{(t)}(\mathbf{x}_t), \mathbf{x}_{\theta^*}^{(t)}(\mathbf{x}_t)$, representing the *estimated* score, noise, and noiseless image, respectively. Sampling from (1) can be implemented by ancestral sampling, which iteratively performs

$$\mathbf{x}_{t-1} = \frac{1}{\sqrt{\alpha_t}} \left(\mathbf{x}_t - \frac{1 - \alpha_t}{\sqrt{1 - \bar{\alpha}_t}} \hat{\epsilon}_t \right) + \tilde{\beta}_t \epsilon, \quad (5)$$

where $\tilde{\beta}_t := \frac{1-\bar{\alpha}_{t-1}}{1-\bar{\alpha}_t} \beta_t$.

One can also view ancestral sampling (5) as solving the reverse generative stochastic differential equation (SDE) of the variance preserving (VP) linear forward SDE [34]. Additionally, one can construct the variance exploding (VE) SDE by setting $q(\mathbf{x}_t|\mathbf{x}_0) = \mathcal{N}(\mathbf{x}_t|\mathbf{x}_0, \sigma_t^2 \mathbf{I})$, which is in a form of Brownian motion.

DDIM Seen either from the variational or the SDE perspective, diffusion models are inevitably slow to sample from. To overcome this issue, DDIM [30] proposes another method of sampling which only requires matching the marginal distributions $q(\mathbf{x}_t|\mathbf{x}_0)$. Specifically, the update rule is given as follows

$$\mathbf{x}_{t-1} = \sqrt{\bar{\alpha}_{t-1}} \hat{\mathbf{x}}_t + \sqrt{1 - \bar{\alpha}_{t-1} - \eta^2 \tilde{\beta}_t^2} \epsilon_{\theta^*}^{(t)}(\mathbf{x}_t) + \eta \tilde{\beta}_t \epsilon, \quad (6)$$

where $\eta \in [0, 1]$ is a parameter controlling the stochasticity of the update rule, and $\hat{\mathbf{x}}_t$ is the *denoised* estimate

$$\hat{\mathbf{x}}_t := \mathbf{x}_{\theta^*}^{(t)}(\mathbf{x}_t) := \frac{1}{\sqrt{\bar{\alpha}_t}} (\mathbf{x}_t - \sqrt{1 - \bar{\alpha}_t} \epsilon_{\theta^*}^{(t)}(\mathbf{x}_t)), \quad (7)$$

which can also be equivalently derived from Tweedie’s formula [11]. In (6), $\eta = 0.0$ leads to fully deterministic sampling, whereas $\eta = 1.0$ with $\tilde{\beta}_t = \sqrt{(1 - \bar{\alpha}_{t-1})/(1 - \bar{\alpha}_t)} \sqrt{1 - \bar{\alpha}_t/\bar{\alpha}_{t-1}}$ recovers the ancestral sampling of DDPMs.

3. Decomposed Diffusion Sampling

In this section, we will begin by examining DDIM to reveal its intriguing geometric decomposition, which can be generalized to accelerate the conditional diffusion sampling process. We defer all proofs in the supplementary section. To begin with, we define some necessary mathematical notation. For a scalar a , points \mathbf{x}, \mathbf{y} , and a set A , we use the following notations. $aA := \{a\mathbf{x} : \mathbf{x} \in A\}$; $d(\mathbf{x}, A) := \inf_{\mathbf{y} \in A} \|\mathbf{x} - \mathbf{y}\|_2$; $B_r(A) := \{\mathbf{x} : d(\mathbf{x}, A) < r\}$.

DDIM decomposition Upon inspection of (6), we can see that DDIM can be decomposed as

$$\mathbf{x}_{t-1} = \text{Denoise}(\mathbf{x}_t, \hat{\mathbf{x}}_t) + \overbrace{\text{Noise}(\mathbf{x}_t, \hat{\mathbf{x}}_t)}^{\tilde{\mathbf{w}}_t} + \eta \tilde{\beta}_t \epsilon \quad (8)$$

where $\tilde{\mathbf{w}}_t$ denotes the total noise and

$$\text{Denoise}(\mathbf{x}_t, \hat{\mathbf{x}}_t) = \sqrt{\bar{\alpha}_{t-1}} \hat{\mathbf{x}}_t \quad (9)$$

$$\text{Noise}(\mathbf{x}_t, \hat{\mathbf{x}}_t) = \sqrt{1 - \bar{\alpha}_{t-1} - \eta^2 \tilde{\beta}_t^2} \hat{\epsilon}_t \quad (10)$$

To gain an intuitive geometric understanding of the two components in (10), we make the following simplifying assumption for the clean data manifold:

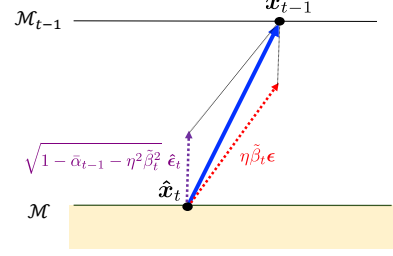


Figure 4: Decomposition of $\tilde{\mathbf{w}}_t$: Noise, pure noise.

Assumption 1 (Strong manifold assumption: subspace structure). *The clean data manifold $\mathcal{M} \subset \mathbb{R}^n$ is a subspace of dimension $l \ll n$. Moreover, the data distribution p_0 is the uniform distribution on the data manifold \mathcal{M} .*

Now, we have the following decomposition:

Proposition 1 (DDIM Decomposition). *Under Assumption 1, we have*

$$\text{Denoise}(\mathbf{x}_t, \hat{\mathbf{x}}_t) = \frac{\sqrt{\bar{\alpha}_{t-1}}}{\sqrt{\bar{\alpha}_t}} \mathcal{P}_{\mathcal{M}} \mathbf{x}_t \quad (11)$$

$$\text{Noise}(\mathbf{x}_t, \hat{\mathbf{x}}_t) = -\frac{\sqrt{1 - \bar{\alpha}_{t-1} - \eta^2 \tilde{\beta}_t^2}}{\sqrt{1 - \bar{\alpha}_t}} \mathcal{P}_{\mathcal{M}}^\perp \mathbf{x}_t \quad (12)$$

where $\mathcal{P}_{\mathcal{M}}$ and $\mathcal{P}_{\mathcal{M}}^\perp$ denotes the orthogonal projection to the subspace \mathcal{M} and its orthogonal complement, respectively.

It’s important to note that the noise component in Equation (10) consists of two parts: 1) $\text{Noise}(\mathbf{x}_t, \hat{\mathbf{x}}_t)$, and 2) fully stochastic noise, denoted as $\eta \tilde{\beta}_t \epsilon$ (See Fig. 4). Proposition 2 shows that these two components form a valid noise component that matches a forward diffusion step [30].

Proposition 2 (Total noise). *Assuming optimality of $\epsilon_{\theta^*}^{(t)}$, the total noise $\tilde{\mathbf{w}}_t$ in (6) can be represented by*

$$\tilde{\mathbf{w}}_t = \sqrt{1 - \bar{\alpha}_{t-1}} \tilde{\epsilon} \quad (13)$$

for some $\tilde{\epsilon} \sim \mathcal{N}(0, \mathbf{I})$. In other words, (10) is equivalently represented by $\mathbf{x}_{t-1} = \sqrt{\bar{\alpha}_{t-1}} \hat{\mathbf{x}}_t + \sqrt{1 - \bar{\alpha}_{t-1}} \tilde{\epsilon}$ for some $\tilde{\epsilon} \sim \mathcal{N}(0, \mathbf{I})$.

DDIM is commonly interpreted as a type of probability flow ODE [34]. Recent works [23, 17, 22] have shown that performance can be further improved by using higher-order solvers, such as Heun’s method, instead of the first-order discretization. However, the ODE interpretation of DDIM is only applicable when $\eta = 0$ and does not generalize to the full range of choices. In contrast, with Proposition 2, it can be seen that the difference between DDIM and DDPM lies only in the degree of dependence on the deterministic estimate of the noise component, with feasible intermediate values $\eta \in (0, 1)$.

In a recent study [7], it was found that, assuming Assumption 1 and utilizing the Gaussian annulus theorem [2], diffusion models possess a shell-like geometric structure. Figure 3 illustrates this structure. Using Proposition 1, this can be stated formally as follows:

Proposition 3 (Concentration of noisy data). *Under Assumption 1, the probability measure $p(\mathbf{x}_{t-1})$ is concentrated on l -dimensional manifold $\mathcal{M}_{t-1} := \{\mathbf{y} \in \mathbb{R}^n : d(\mathbf{y}, \mathcal{M}) = r_{t-1} := \sqrt{(1 - \bar{\alpha}_t)(n - l)}\}$. Rigorously, $p(B_{\epsilon r_{t-1}}(\mathcal{M}_{t-1})) > 1 - \delta$, for some small $\epsilon, \delta > 0$.*

Figure 3(a) illustrates our geometric insight into the unconditional DDIM sampling process. First, in the Denoise() step, we project $\mathbf{x}_t \in \mathcal{M}_t$ onto the clean data manifold with proper scaling. Next, we add noise components of variance $1 - \bar{\alpha}_{t-1}$ to transfer the denoised sample to the next noisy shell-like manifold, \mathcal{M}_{t-1} . The direction of this transition to \mathcal{M}_{t-1} is determined by the vector sum of the component orthogonal to the data manifold and the stochastic directional component, $\eta \tilde{\beta}_t \epsilon$ (See Fig. 4).

Conditional diffusion for inverse problem Consider a typical linear inverse problem

$$\mathbf{y} = \mathbf{A}\mathbf{x} \quad (14)$$

where \mathbf{A} is the linear mapping and the goal is to retrieve \mathbf{x} from the measurement \mathbf{y} . Without loss of generality, we assume that \mathbf{A} is symmetric.² Most of the conditional diffusion sampling for inverse problems [18, 5, 6] uses standard reverse diffusion (e.g. (5)), alternated with an operation to impose data consistency (DC):

$$\mathbf{x}'_t = \mathbf{F}(\mathbf{x}_t) \quad (15)$$

where $\mathbf{F}(\cdot)$ denotes a DC mapping. Note that our parameterized score function $\epsilon_{\theta^*}^{(t)}(\mathbf{x}_t)$ is also a function of t , and is trained with samples supported on \mathcal{M}_t . Not surprisingly, $\epsilon_{\theta^*}^{(t)}$ shows good performance on denoising $\mathbf{x}_t \sim \mathcal{M}_t$, but fails at a sample $\mathbf{x}'_t \notin \mathcal{M}_t$. Hence, if conditioning is imposed *after* an unconditional update step as in (15), even if \mathbf{x}_t is supported on \mathcal{M}_t , the updated sample \mathbf{x}'_t may not be able to keep the intermediate reconstruction \mathbf{x}'_t on the manifold, leading to the error in the next application of the score function (See Figure 3(b)).

Using this geometric perspective, it is desirable to keep the sample \mathbf{x}_{t-1} on the noisy manifold \mathcal{M}_{t-1} when developing a solver and to use it as input for the next application of ϵ_{θ^*} . In the proposed decomposed diffusion sampling (DDS), this goal can be accomplished by employing optimization techniques that ensure the updates from the denoised image

²Otherwise, we can obtain an equivalent inverse problem with symmetric linear mapping $\tilde{\mathbf{A}}$ as $\tilde{\mathbf{y}} := \mathbf{A}^* \mathbf{y} = \mathbf{A}^* \mathbf{A} \mathbf{x} := \tilde{\mathbf{A}} \mathbf{x}$.

$\hat{\mathbf{x}}_t \in \mathcal{M}$ remain on the clean manifold. Noise() can then be used to ensure the transition to the noisy manifold \mathcal{M}_{t-1} (See Figure 3(c)).

In a related strategy used in [7], the manifold constrained gradient (MCG) was employed, where the updated estimate from the noisy sample $\mathbf{x}_t \in \mathcal{M}_t$ is constrained to stay on the same noisy manifold \mathcal{M}_t . This is achieved by computing the MCG on a noisy sample $\mathbf{x}_t \in \mathcal{M}_t$ for a given loss function $\ell(\mathbf{x})$ as $\nabla_{\mathbf{x}_t}^{m\text{cg}} \ell(\mathbf{x}_t) = \nabla_{\mathbf{x}_t} \ell(\hat{\mathbf{x}}_t(\mathbf{x}_t))$, where $\hat{\mathbf{x}}_t(\mathbf{x}_t)$ is again the denoised sample from \mathbf{x}_t through Tweedie's formula. Unfortunately, the computation of MCG requires computationally expensive backpropagation.

Lemma 1 makes a significant contribution by demonstrating that on the clean manifold, it is unnecessary to compute the MCG. Instead, the standard conjugate gradient (CG) method is sufficient to ensure that the updated samples remain on the clean manifold.

Lemma 1 (CG on the Clean Manifold). *For the given inverse problem (14), suppose that the clean manifold \mathcal{M} is given by the l -th order Krylov subspace \mathcal{K}_l [21], i.e.*

$$\mathcal{M} = \mathcal{K}_l = \text{Span}(\mathbf{y}, \mathbf{A}\mathbf{y}, \dots, \mathbf{A}^{l-1}\mathbf{y}) \quad (16)$$

Let $\hat{\mathbf{x}}_t^{(i)}$ denote the CG update for (14) starting with $\hat{\mathbf{x}}_t^{(0)} = \hat{\mathbf{x}}_t$. Then, we have $\hat{\mathbf{x}}_t^{(i)} \in \mathcal{M}$, $i = 1, \dots, p \leq l$.

Recall that Krylov space is a frequently used subspace for inverse problems [21]. Under this assumption, we can obtain our key result in this paper.

Theorem 1 (VP-DDS). *Suppose that $\mathcal{M} = \mathcal{K}_l$ and \mathbf{x}_t lies on the noisy manifold \mathcal{M}_t . Consider the DDS update:*

$$\mathbf{x}_{t-1} = \text{CDenoise}(\mathbf{x}_t, \hat{\epsilon}_t) + \text{Noise}(\mathbf{x}_t, \hat{\epsilon}_t) + \eta \tilde{\beta}_t \epsilon \quad (17)$$

where the function $\text{CDenoise}(\mathbf{x}_t, \hat{\epsilon}_t)$ is defined as

$$\text{CDenoise}(\mathbf{x}_t, \hat{\epsilon}_t) = \sqrt{\bar{\alpha}_{t-1}} \text{CG}^{(p)}(\hat{\mathbf{x}}_t), \quad p \leq l \quad (18)$$

and $\text{CG}^{(p)}(\hat{\mathbf{x}}_t)$ denotes the p -th CG update for (14) starting from $\hat{\mathbf{x}}_t$. Then, we can conclude that \mathbf{x}_{t-1} belongs to the noisy manifold \mathcal{M}_{t-1} .

Extension to VE-SDE For score functions trained in the context of DDPM (VP-SDE), DDIM sampling of (6) can directly be used. However, for VE-SDE that was not developed under the variational framework, it is unclear how to construct a sampler equivalent of DDIM for VP-SDE. As one of our goals is to enable the direct adoption of pre-trained diffusion models regardless of the framework, our goal is to devise a fast sampler tailored for VE-SDE. Now, the idea of the decomposition of DDIM steps can be easily adopted to address this issue.

First, observe that the forward conditional density for VE-SDE can be written as $q(\mathbf{x}_t | \mathbf{x}_0) = \mathcal{N}(\mathbf{x}_t | \mathbf{x}_0, \sigma_t^2 \mathbf{I})$, where σ_t is taken to be a geometric series following [34]. This directly leads to the following result:

Proposition 4 (VE Decomposition). *The following update rule recovers a sample from the marginal $q(\mathbf{x}_{t-1}|\mathbf{x}_0) \forall \eta \in [0, 1]$.*

$$\mathbf{x}_{t-1} = \text{Denoise}(\mathbf{x}_t, \hat{\mathbf{s}}_t) + \overbrace{\text{Noise}(\mathbf{x}_t, \hat{\mathbf{s}}_t) + \sigma_{t-1}\eta\tilde{\beta}_t\epsilon}^{\tilde{w}_t} \quad (19)$$

where

$$\text{Denoise}(\mathbf{x}_t, \hat{\mathbf{s}}_t) = \hat{\mathbf{x}}_t := \mathbf{x}_t + \sigma_t^2 \hat{\mathbf{s}}_t \quad (20)$$

$$\text{Noise}(\mathbf{x}_t, \hat{\mathbf{s}}_t) = -\sigma_{t-1}\sigma_t \sqrt{1 - \tilde{\beta}^2\eta^2} \hat{\mathbf{s}}_t \quad (21)$$

Again, $\hat{\mathbf{x}}_t$ arises from Tweedie’s formula. With $\eta = 1$ and $\tilde{\beta} = 1 - \sigma_{t-1}^2/\sigma_t^2$, we can recover the original VE-SDE, whereas $\eta = 0$ leads to the deterministic variation of VE-SDE, which we call VE-DDIM. We can now use the usual VP-DDIM (6) or VE-DDIM (19) depending on the training strategy of the pre-trained score function. Arguments based on VE-SDE can be made analogous to Proposition 1 and Theorem 1. See appendix A for details.

Application to inverse problems One of the most widely used optimization methods is based on the proximal optimization [26]. Here, the proximal mapping of a convex function h is given as

$$\text{prox}_h(\mathbf{x}) = \arg \min_{\mathbf{u}} h(\mathbf{u}) + \frac{1}{2} \|\mathbf{u} - \mathbf{x}\|^2 \quad (22)$$

Then, the update step using the proximal mapping is implemented as

$$\hat{\mathbf{x}}'_t = \text{prox}_h(\hat{\mathbf{x}}_t) \quad (23)$$

For example, to find the proximal mapping for the inverse problem (14), we define $h(\mathbf{u}) = \iota_C(\mathbf{u})$, where ι_C denotes the indicator function for the set C and

$$C = \{\mathbf{u} : \mathbf{y} = \mathbf{A}\mathbf{u}\} \quad (24)$$

Then, the corresponding proximal mapping from the denoised sample $\hat{\mathbf{x}}_t$ is given by the projection on the set C , $P_C(\hat{\mathbf{x}}_t)$ [26]

$$\begin{aligned} \hat{\mathbf{x}}'_t &= \text{prox}_h(\hat{\mathbf{x}}_t) = P_C(\hat{\mathbf{x}}_t) \\ &= (\mathbf{I} - \mathbf{A}^\dagger \mathbf{A})\hat{\mathbf{x}}_t + \mathbf{A}^\dagger \mathbf{y}, \end{aligned} \quad (25)$$

where \mathbf{A}^\dagger denotes the pseudo-inverse of \mathbf{A} . In fact, this is equivalent to the update equation of DDNM [37] for noiseless image restoration problems. Unfortunately, the one-step update equation (25) in DDNM does not ensure that the update signal $\hat{\mathbf{x}}'_t$ lies in the clean data manifold $\mathcal{M} = \mathcal{K}_l$ for $l \ll n$ (See Figure 3(b)).

Instead, one can perform conjugate gradient (CG) [29] by initializing the process with $\hat{\mathbf{x}}_t$, which would induce

smoother (iterative) transitions to the projection point (See Figure 3(c)). Here, we empirically find that CG outperforms naive projections (25) by quite large margins, confirming our theoretical finding in Lemma 1 and Theorem 1, 2. This is to be expected, as using p -step iterations of CG with $p \leq l$ enforces the update $\hat{\mathbf{x}}_t^{(p)}$ to stay on the clean manifold $\mathcal{M} = \mathcal{K}_l$ whereas the orthogonal projections in DDNM do not guarantee (Compare Fig. 3(b), Fig. 3(c); See appendix B for detailed implementation) this property.

Furthermore, our CG step can be easily extended for noisy image restoration problems. Unlike DDNM approach that relies on the singular value decomposition to handle noise, which is non-trivial to perform on forward operators in medical imaging (e.g. PI CS-MRI, CT), in our method we can simply choose $h(\mathbf{u})$ in (22) as:

$$h(\mathbf{u}) = \frac{\gamma}{2} \|\mathbf{y} - \mathbf{A}\mathbf{u}\|^2 \quad (26)$$

and perform CG iteration up to $p \leq l$. Finally, our method can also be readily extended to accelerate DiffusionMBIR [6] for 3D CT reconstruction by adhering to the same principles. Specifically, we implement the following optimization strategy to impose the conditioning:

$$\min_{\mathbf{x}} \frac{1}{2} \|\mathbf{A}\mathbf{x} - \mathbf{y}\|_2^2 + \lambda \|\mathbf{D}_z \mathbf{x}\|_1, \quad (27)$$

where \mathbf{D}_z is the finite difference operator that is applied to the z -axis that is not learned through the diffusion prior. As the additional prior is only imposed in the direction that is orthogonal to the axial slice dimension (xy) captured by the diffusion prior (i.e. manifold \mathcal{M}), (27) can be solved effectively with the alternating direction method of multipliers (ADMM) [3] using CG steps after obtaining 3D $\hat{\mathbf{x}}_t$ by applying Tweedie’s denoising formula slice by slice.

4. Experiments

Problem setting. We have the following general measurement model

$$\mathbf{y} = \mathbf{P}\mathbf{T}\mathbf{S}\mathbf{x} =: \mathbf{A}\mathbf{x}, \mathbf{y} \in \mathbb{C}^n, \mathbf{A} \in \mathbb{C}^{n \times d}, \quad (28)$$

where \mathbf{P} is the sub-sampling matrix, \mathbf{T} is the discrete transform matrix (i.e. Fourier, Radon), and $\mathbf{S} = \mathbf{I}$ when we have a single-array measurement including CT, and $\mathbf{S} = [\mathbf{S}^{(1)}, \dots, \mathbf{S}^{(c)}]$ when we have a c -coil PI measurement.

We conduct experiments on two distinguished applications—accelerated MRI, and 3D CT reconstruction. For the former, we follow the evaluation protocol of [9] and test our method on the fastMRI knee dataset [39] on diverse sub-sampling patterns. We provide comparisons against representative DIS methods Score-MRI [9], Jalal *et al.* [15]; Strong supervised learning baselines: E2E-Varnet [35],

Mask Pattern	Acc.		TV [1]	Supervised U-Net [39]	E2E-Varnet [35]	Jalal <i>et al.</i> [15] (2100)	Score-MRI [9] (4000 \times 2 \times C*)	DDS VP (99)	DDS VP (49)	DDS VP (19)
Uniform 1D	$\times 4$	PSNR [db]	27.32	31.77	32.96	32.49	33.25	34.88	34.61	32.73
		SSIM	0.662	0.846	0.856	0.868	0.857	0.954	0.956	0.927
	$\times 8$	PSNR [db]	25.02	29.51	31.98	32.19	32.01	31.62	30.16	30.33
		SSIM	0.532	0.780	0.828	0.835	0.821	0.876	0.830	0.891
Gaussian 1D	$\times 4$	PSNR [db]	30.55	32.66	34.15	33.98	34.25	35.12	35.15	34.63
		SSIM	0.789	0.866	0.878	0.881	0.885	0.963	0.961	0.957
	$\times 8$	PSNR [db]	27.98	31.64	33.15	32.76	32.43	33.27	33.43	32.83
		SSIM	0.747	0.841	0.868	0.870	0.855	0.937	0.947	0.940
Gaussian 2D	$\times 8$	PSNR [db]	29.20	24.51	20.97	30.97	31.43	33.99	34.55	32.55
		SSIM	0.781	0.724	0.642	0.812	0.831	0.948	0.956	0.916
	$\times 15$	PSNR [db]	26.28	14.93	16.66	27.34	29.17	27.86	25.75	25.66
		SSIM	0.547	0.372	0.435	0.692	0.704	0.732	0.695	0.693
VD Poisson disk	$\times 8$	PSNR [db]	29.52	20.89	20.70	32.60	31.98	35.31	35.36	35.39
		SSIM	0.562	0.576	0.592	0.833	0.816	0.897	0.875	0.915
	$\times 15$	PSNR [db]	26.19	16.01	18.82	30.22	29.59	34.84	35.18	34.59
		SSIM	0.510	0.537	0.548	0.749	0.702	0.934	0.931	0.940

Table 1: Quantitative metrics for noiseless parallel imaging reconstruction. Numbers in parenthesis: NFE. *: expressed as $\times 2 \times C$ as the network is evaluated for real/imag part of each coil. **Bold**: best.

U-Net [39]; compressed sensing baseline total variation reconstruction [1].

For the latter, we follow [6] and test both sparse-view CT reconstruction (SV-CT), and limited angle CT reconstruction (LA-CT) on the AAPM 256 \times 256 dataset. We compare against representative DIS methods DiffusionMBIR [6] and Chung *et al.* [7]; Supervised baselines Lahiri *et al.* [20] and FBPCovNet [16]; Compressed sensing baseline ADMM-TV. For all proposed methods, we employ $M = 5$, $\eta = 0.15$ for 19 NFE, $\eta = 0.5$ for 49 NFE, $\eta = 0.8$ for 99 NFE unless specified otherwise. For PI CS-MRI experiments, we employ the rejection sampling based on a residual-based criterion to ensure stability. Further experimental details can be found in appendix F.

	Score-MRI	DDNM [37]	DDS (ours)				
			1	3	5	10	20
PSNR[db]	26.48	31.36	31.51	33.78	34.61	32.48	25.56
SSIM	0.688	0.932	0.934	0.952	0.956	0.873	0.650

Table 2: Ablation study on the DC strategy. 49 NFE VP DDIM sampling strategy, uniform 1D $\times 4$ acc. reconstruction.

4.1. Accelerated MRI

Improvement over DDNM. Fixing the sampling strategy the same, we inspect the effect of the three different data consistency imposing strategies: Score-MRI [9], DDNM [37], and DDS. For DDS, we additionally search for the optimal number of CG iterations per sampling step. In Tab. 2, we see that under the low NFE regime, the score-MRI DC strategy has significantly worse performance than the proposed methods, even when using the same DDIM sampling strategy. Moreover, we see that overall, DDS outperforms DDNM by a few db in PSNR. We see that 5 CG iterations per denoising step strike a good balance. However, care must be

taken as one should not attempt to use CG iterations of more than 10, which is the usual setting for most model-based iterative reconstruction methods. We conjecture that when using too many iterations for CG, the samples may fall off the data manifold \mathcal{M} , hence resulting in worse performance. One might question the additional computational overhead of introducing the iterative CG into the already slow diffusion sampling. Nonetheless, from our experiments, we see that on average, a single CG iteration takes about 0.004 sec. Consequently, it only takes about 0.2 sec more than the analytic counterpart when using 50 NFE (Analytic: 4.51 sec vs. CG(5): 4.71 sec.).

Improvement on VE [9]. Keeping the pre-trained model intact from [9], we switch from the Score-MRI sampling to Algorithm 4, and report on the reconstruction results from uniform 1D $\times 4$ accelerated measurements in Tab. E.2. Note that Score-MRI uses 2000 PC as the default setting, which amounts to 4000 NFE, reaching 33.25 PSNR. We see almost no degradation in quality down to 200 NFE, but the performance rapidly degrades as we move down to 100, and completely fails when we set the NFE ≤ 50 . On the other hand, by switching to the proposed solver, we are able to achieve the reconstruction quality that *better than* Score-MRI (4000 NFE) with only 100 NFE sampling. Moreover, we see that we can reduce the NFE down to 30 and still achieve decent reconstructions. This is a useful property for a reconstruction algorithm, as we can trade off reconstruction quality with speed. However, we observe several downsides of using the VE parameterization including numerical instability with large NFE, which we analyze in detail in appendix E.

Parallel Imaging with VP parameterization. (Noiseless) We conduct thorough PI reconstruction experiments with 4 different types of sub-sampling patterns following [9]. Algorithm 1 in supplementary material is used for all experiments. Quantitative results are shown in Tab. 1 (Also see

Method	8-view						4-view						2-view					
	Axial*		Coronal		Sagittal		Axial*		Coronal		Sagittal		Axial*		Coronal		Sagittal	
	PSNR \uparrow	SSIM \uparrow																
DDS VP (19)	32.31	0.904	35.82	0.975	33.03	0.931	30.59	0.906	30.38	0.947	27.90	0.903	25.43	0.844	24.38	0.862	22.10	0.769
DDS VP (49)	33.86	0.930	35.39	0.974	32.97	0.937	31.48	0.918	30.81	0.949	28.43	0.900	25.85	0.857	24.60	0.871	22.69	0.791
DDS VE (99)	33.43	0.932	34.35	0.972	32.01	0.935	31.23	0.915	30.62	0.958	28.52	0.914	25.09	0.833	24.15	0.855	22.26	0.785
DiffusionMBIR [6] (4000)	33.49	0.942	35.18	0.967	32.18	0.910	30.52	0.914	30.09	0.938	27.89	0.871	24.11	0.810	23.15	0.841	21.72	0.766
Chung <i>et al.</i> [7] (4000)	28.61	0.873	28.05	0.884	24.45	0.765	27.33	0.855	26.52	0.863	23.04	0.745	24.69	0.821	23.52	0.806	20.71	0.685
Lahiri <i>et al.</i> [20]	21.38	0.711	23.89	0.769	20.81	0.716	20.37	0.652	21.41	0.721	18.40	0.665	19.74	0.631	19.92	0.720	17.34	0.650
FBPConvNet [16]	16.57	0.553	19.12	0.774	18.11	0.714	16.45	0.529	19.47	0.713	15.48	0.610	16.31	0.521	17.05	0.521	11.07	0.483
ADMM-TV	16.79	0.645	18.95	0.772	17.27	0.716	13.59	0.618	15.23	0.682	14.60	0.638	10.28	0.409	13.77	0.616	11.49	0.553

Table 3: Quantitative evaluation of SV-CT on the AAPM 256 \times 256 test set. (Numbers in parenthesis): NFE, **Bold**: best.

Fig. G.1 for qualitative results). As the proposed method is based on diffusion models, it is agnostic to the sub-sampling patterns, generalizing well to all the different sampling patterns, whereas supervised learning-based methods such as U-Net and E2E-Varnet fail dramatically on 2D subsampling patterns.

In Tab. 1, we see that DDS sets the new state-of-the-art in most cases even when the NFE is constrained to < 100 . Note that this is a dramatic improvement over the previous method [9], as for parallel imaging, Score-MRI required 120k ($C = 15$) NFE for the reconstruction of a single image. Contrarily, DDS is able to *outperform* score-MRI with 49 NFE, and performs *on par* with score-MRI with 19 NFE. Even disregarding the additional $\times 2C$ more NFEs required for score-MRI to account for the multi-coil complex valued acquisition, the proposed method still achieves $\times 80 \sim \times 200$ acceleration. We note that on average, our method takes about 4.7 seconds for 49 NFE, and about 2.25 seconds for 19 NFE on a single commodity GPU (RTX 3090).

Mask Pattern	Acc.	TV	DPS [5] (1000)	DDS VP (49)
Uniform 1D	$\times 4$	PSNR [db]	24.19	24.40
		SSIM	0.687	0.656
	$\times 8$	PSNR [db]	23.02	24.60
		SSIM	0.638	0.666
VD Poisson disk	$\times 8$	PSNR [db]	23.07	23.48
		SSIM	0.609	0.592
	$\times 15$	PSNR [db]	20.92	23.57
		SSIM	0.554	0.622

Table 4: Quantitative metrics for **noisy** parallel imaging reconstruction. Numbers in parenthesis: NFE.

Noisy multi-coil MRI reconstruction. One of the most intriguing properties of the proposed DDS is the ease of handling measurement noise without careful computation of singular value decomposition (SVD), which is non-trivial to perform for our tasks. With (26), we can solve the proximal solution with CG, arriving at Algorithm 2 in supplementary material. For comparison, methods that try to cope with measurement noise via SVD in the diffusion model context [18, 37] are not applicable and cannot be compared. One work that does not require computation of SVD and hence is applicable is DPS [5] relying on backpropagation. To test the efficacy of DDS on noisy inverse problems, we

add a rather heavy complex Gaussian noise ($\sigma = 0.05$) to the k -space multi-coil measurements and reconstruct with Algorithm 2 by setting $\gamma = 0.95$ found through grid search.

In Tab. 4, we see that DDS far outperforms DPS [5] with 1000 NFE by a large margin, while being about $\times 40$ faster as DPS requires the heavy computation of backpropagation.

4.2. 3D CT reconstruction

Sparse-view CT. Similar to the accelerated MRI experiments, we aim to both 1) improve the original VE model of [6], and 2) train a new VP model better suitable for DDS. Inspecting Tab. 3, we see that by using Algorithm 5 in supplementary material, we are able to reduce the NFE to 100 and still achieve results that are on par with DiffusionMBIR with 4000 NFE. However, we observe similar instabilities with the VE parameterization. Additionally, we find it crucial to initialize the optimization process with CG and later switch to ADMM-TV using a CG solver for proper convergence (see appendix D.2 for discussion). Switching to the VP parameterization and using Algorithm 3, we now see that DDS achieves the new state-of-the-art with ≤ 49 NFE. Notably, this decreases the sampling time to ~ 25 min for 49 NFE, and ~ 10 min wall-clock time for 19 NFE on a single RTX 3090 GPU, compared to the painful 2 days for DiffusionMBIR. In Tab. E.3, we see similar improvements that were seen from SV-CT, where DDS significantly outperforms DiffusionMBIR while being several orders of magnitude faster.

5. Conclusion

In this work, we present Decomposed Diffusion Sampling (DDS), a general DIS for challenging real-world medical imaging inverse problems. Leveraging the geometric view of diffusion models and the property of the CG solvers on the clean manifold, we show that performing numerical optimization schemes on the denoised representation is superior to the previous methods of imposing DC. Further, we devise a fast sampler based on DDIM that works well for both VE/VP settings. With extensive experiments on multi-coil MRI reconstruction and 3D CT reconstruction, we show that DDS achieves superior quality while being $\geq \times 80$ faster than the previous DIS.

References

- [1] Kai Tobias Block, Martin Uecker, and Jens Frahm. Under-sampled radial MRI with multiple coils. Iterative image reconstruction using a total variation constraint. *Magnetic Resonance in Medicine: An Official Journal of the International Society for Magnetic Resonance in Medicine*, 57(6):1086–1098, 2007. 7
- [2] Avrim Blum, John Hopcroft, and Ravindran Kannan. *Foundations of data science*. Cambridge University Press, 2020. 5
- [3] Stephen Boyd, Neal Parikh, and Eric Chu. *Distributed optimization and statistical learning via the alternating direction method of multipliers*. Now Publishers Inc, 2011. 6
- [4] Guangyong Chen, Fengyuan Zhu, and Pheng Ann Heng. An efficient statistical method for image noise level estimation. In *Proceedings of the IEEE International Conference on Computer Vision*, pages 477–485, 2015. 15
- [5] Hyungjin Chung, Jeongsol Kim, Michael Thompson Mccann, Marc Louis Klasky, and Jong Chul Ye. Diffusion posterior sampling for general noisy inverse problems. In *International Conference on Learning Representations*, 2023. 3, 5, 8, 14, 15, 19
- [6] Hyungjin Chung, Dohoon Ryu, Michael T Mccann, Marc L Klasky, and Jong Chul Ye. Solving 3d inverse problems using pre-trained 2d diffusion models. *IEEE/CVF Conference on Computer Vision and Pattern Recognition*, 2023. 1, 5, 6, 7, 8, 15, 16, 17
- [7] Hyungjin Chung, Byeongsu Sim, Dohoon Ryu, and Jong Chul Ye. Improving diffusion models for inverse problems using manifold constraints. In Alice H. Oh, Alekh Agarwal, Danielle Belgrave, and Kyunghyun Cho, editors, *Advances in Neural Information Processing Systems*, 2022. 1, 2, 3, 5, 7, 8, 12, 16, 17
- [8] Hyungjin Chung, Byeongsu Sim, and Jong Chul Ye. Come-Closer-Diffuse-Faster: Accelerating Conditional Diffusion Models for Inverse Problems through Stochastic Contraction. In *Proceedings of the IEEE/CVF Conference on Computer Vision and Pattern Recognition*, 2022. 16
- [9] Hyungjin Chung and Jong Chul Ye. Score-based diffusion models for accelerated mri. *Medical Image Analysis*, page 102479, 2022. 1, 6, 7, 8, 13, 14, 15, 16, 17, 18
- [10] Prafulla Dhariwal and Alexander Quinn Nichol. Diffusion models beat GANs on image synthesis. In A. Beygelzimer, Y. Dauphin, P. Liang, and J. Wortman Vaughan, editors, *Advances in Neural Information Processing Systems*, 2021. 2, 17
- [11] Bradley Efron. Tweedie’s formula and selection bias. *Journal of the American Statistical Association*, 106(496):1602–1614, 2011. 4
- [12] Jonathan Ho, Ajay Jain, and Pieter Abbeel. Denoising diffusion probabilistic models. *Advances in Neural Information Processing Systems*, 33:6840–6851, 2020. 1, 3
- [13] Jonathan Ho and Tim Salimans. Classifier-free diffusion guidance. *arXiv preprint arXiv:2207.12598*, 2022. 2
- [14] Aapo Hyvärinen and Peter Dayan. Estimation of non-normalized statistical models by score matching. *Journal of Machine Learning Research*, 6(4), 2005. 3
- [15] Ajil Jalal, Marius Arvinte, Giannis Daras, Eric Price, Alexandros G Dimakis, and Jonathan Tamir. Robust compressed sensing mri with deep generative priors. *Advances in Neural Information Processing Systems*, 34, 2021. 1, 6, 7, 14, 15, 16, 17
- [16] Kyong Hwan Jin, Michael T McCann, Emmanuel Froustey, and Michael Unser. Deep convolutional neural network for inverse problems in imaging. *IEEE Transactions on Image Processing*, 26(9):4509–4522, 2017. 7, 8, 17
- [17] Tero Karras, Miika Aittala, Timo Aila, and Samuli Laine. Elucidating the design space of diffusion-based generative models. In *Proc. NeurIPS*, 2022. 2, 4
- [18] Bahjat Kawar, Michael Elad, Stefano Ermon, and Jiaming Song. Denoising diffusion restoration models. In Alice H. Oh, Alekh Agarwal, Danielle Belgrave, and Kyunghyun Cho, editors, *Advances in Neural Information Processing Systems*, 2022. 1, 2, 5, 8, 14
- [19] Dongjun Kim, Seungjae Shin, Kyungwoo Song, Wanmo Kang, and Il-Chul Moon. Soft truncation: A universal training technique of score-based diffusion model for high precision score estimation. *International conference on machine learning*, 2022. 16
- [20] Anish Lahiri, Marc Klasky, Jeffrey A Fessler, and Saiprasad Ravishankar. Sparse-view cone beam ct reconstruction using data-consistent supervised and adversarial learning from scarce training data. *arXiv preprint arXiv:2201.09318*, 2022. 7, 8, 16, 17
- [21] Jörg Liesen and Zdenek Strakos. *Krylov subspace methods: principles and analysis*. Oxford University Press, 2013. 3, 5, 12
- [22] Luping Liu, Yi Ren, Zhijie Lin, and Zhou Zhao. Pseudo numerical methods for diffusion models on manifolds. In *International Conference on Learning Representations*, 2022. 2, 4
- [23] Cheng Lu, Yuhao Zhou, Fan Bao, Jianfei Chen, Chongxuan Li, and Jun Zhu. DPM-solver: A fast ODE solver for diffusion probabilistic model sampling in around 10 steps. In *Advances in Neural Information Processing Systems*, 2022. 2, 4
- [24] Cheng Lu, Yuhao Zhou, Fan Bao, Jianfei Chen, Chongxuan Li, and Jun Zhu. Dpm-solver++: Fast solver for guided sampling of diffusion probabilistic models. *arXiv preprint arXiv:2211.01095*, 2022. 2
- [25] Chenlin Meng, Ruiqi Gao, Diederik P Kingma, Stefano Ermon, Jonathan Ho, and Tim Salimans. On distillation of guided diffusion models. *arXiv preprint arXiv:2210.03142*, 2022. 2
- [26] Neal Parikh and Stephen Boyd. Proximal algorithms. *Foundations and Trends in optimization*, 1(3):127–239, 2014. 6, 15
- [27] Matteo Ronchetti. Torchraddon: Fast differentiable routines for computed tomography. *arXiv preprint arXiv:2009.14788*, 2020. 16
- [28] Tim Salimans and Jonathan Ho. Progressive distillation for fast sampling of diffusion models. In *International Conference on Learning Representations*, 2022. 2
- [29] Jonathan Richard Shewchuk et al. An introduction to the conjugate gradient method without the agonizing pain, 1994. 6

- [30] Jiaming Song, Chenlin Meng, and Stefano Ermon. Denoising diffusion implicit models. In *9th International Conference on Learning Representations, ICLR*, 2021. 2, 4, 16
- [31] Jiaming Song, Arash Vahdat, Morteza Mardani, and Jan Kautz. Pseudoinverse-guided diffusion models for inverse problems. In *International Conference on Learning Representations*, 2023. 2
- [32] Yang Song and Stefano Ermon. Generative modeling by estimating gradients of the data distribution. In *Advances in Neural Information Processing Systems*, volume 32, 2019. 3
- [33] Yang Song, Liyue Shen, Lei Xing, and Stefano Ermon. Solving inverse problems in medical imaging with score-based generative models. In *International Conference on Learning Representations*, 2022. 1, 13, 17
- [34] Yang Song, Jascha Sohl-Dickstein, Diederik P. Kingma, Abhishek Kumar, Stefano Ermon, and Ben Poole. Score-based generative modeling through stochastic differential equations. In *9th International Conference on Learning Representations, ICLR*, 2021. 1, 2, 4, 5, 17
- [35] Anuroop Sriram, Jure Zbontar, Tullie Murrell, Aaron Defazio, C Lawrence Zitnick, Nafissa Yakubova, Florian Knoll, and Patricia Johnson. End-to-end variational networks for accelerated MRI reconstruction. In *International Conference on Medical Image Computing and Computer-Assisted Intervention*, pages 64–73. Springer, 2020. 6, 7, 17, 18
- [36] Martin Uecker, Peng Lai, Mark J Murphy, Patrick Virtue, Michael Elad, John M Pauly, Shreyas S Vasanaawala, and Michael Lustig. ESPIRiT—an eigenvalue approach to autocalibrating parallel MRI: where SENSE meets GRAPPA. *Magnetic resonance in medicine*, 71(3):990–1001, 2014. 16, 17
- [37] Yinhuai Wang, Jiwen Yu, and Jian Zhang. Zero-shot image restoration using denoising diffusion null-space model. In *The Eleventh International Conference on Learning Representations*, 2023. 2, 3, 6, 7, 8, 15
- [38] Suttisak Wizadwongsa and Supasorn Suwajanakorn. Accelerating guided diffusion sampling with splitting numerical methods. In *The Eleventh International Conference on Learning Representations*, 2023. 2
- [39] Jure Zbontar, Florian Knoll, Anuroop Sriram, Tullie Murrell, Zhengnan Huang, Matthew J Muckley, Aaron Defazio, Ruben Stern, Patricia Johnson, Mary Bruno, et al. fastMRI: An open dataset and benchmarks for accelerated MRI. *arXiv preprint arXiv:1811.08839*, 2018. 1, 6, 7, 16, 18
- [40] Kai Zhang, Wangmeng Zuo, Yunjin Chen, Deyu Meng, and Lei Zhang. Beyond a gaussian denoiser: Residual learning of deep CNN for image denoising. *IEEE transactions on image processing*, 26(7):3142–3155, 2017. 16, 17

Appendix

A. Proofs

Proposition 1 (DDIM Decomposition). *Under Assumption 1, we have*

$$\text{Denoise}(\mathbf{x}_t, \hat{\epsilon}_t) = \frac{\sqrt{\bar{\alpha}_{t-1}}}{\sqrt{\bar{\alpha}_t}} \mathcal{P}_{\mathcal{M}} \mathbf{x}_t \quad (11)$$

$$\text{Noise}(\mathbf{x}_t, \hat{\epsilon}_t) = -\frac{\sqrt{1 - \bar{\alpha}_{t-1} - \eta^2 \tilde{\beta}_t^2}}{\sqrt{1 - \bar{\alpha}_t}} \mathcal{P}_{\mathcal{M}}^\perp \mathbf{x}_t \quad (12)$$

where $\mathcal{P}_{\mathcal{M}}$ and $\mathcal{P}_{\mathcal{M}}^\perp$ denotes the orthogonal projection to the subspace \mathcal{M} and its orthogonal complement, respectively.

Proof. Thanks to the forward sampling $\mathbf{x}_{t-1} = \sqrt{\bar{\alpha}_{t-1}} \mathbf{x}_0 + \sqrt{1 - \bar{\alpha}_{t-1}} \tilde{\epsilon}$, we can obtain the closed-form expression of the likelihood:

$$p(\mathbf{x}_t | \mathbf{x}_0) = \frac{1}{(2\pi(1 - \bar{\alpha}(t)))^{d/2}} \exp\left(-\frac{\|\mathbf{x}_t - \sqrt{\bar{\alpha}(t)} \mathbf{x}_0\|^2}{2(1 - \bar{\alpha}(t))}\right), \quad (29)$$

which is a Gaussian distribution. Using the Bayes' theorem, we have

$$p(\mathbf{x}_t) = \int p(\mathbf{x}_t | \mathbf{x}_0) p(\mathbf{x}_0) d\mathbf{x}_0. \quad (30)$$

According to Assumption 1, $p(\mathbf{x}_0)$ is a uniform distribution on the subspace \mathcal{M} . To incorporate this in (30), we first compute $p(\mathbf{x}_t)$ by modeling $p(\mathbf{x}_0)$ as the zero-mean Gaussian distribution with the isotropic variance σ^2 and then take the limit $\sigma \rightarrow \infty$. More specifically, we have

$$p(\mathbf{x}_0) = \frac{1}{(2\pi\sigma^2)^{l/2}} \exp\left(-\frac{\|\mathcal{P}_{\mathcal{M}} \mathbf{x}_0\|^2}{2\sigma^2}\right), \quad (31)$$

where we use $\mathcal{P}_{\mathcal{M}} \mathbf{x}_0 = \mathbf{x}_0$ as $\mathbf{x}_0 \in \mathcal{M}$. Therefore, we have

$$\begin{aligned} p(\mathbf{x}_t, \mathbf{x}_0) &= p(\mathbf{x}_t | \mathbf{x}_0) p(\mathbf{x}_0) \\ &= \frac{1}{(2\pi(1 - \bar{\alpha}(t)))^{d/2}} \frac{1}{(2\pi\sigma^2)^{l/2}} \exp(-d(\mathbf{x}_t, \mathbf{x}_0)) \end{aligned}$$

where

$$\begin{aligned} d(\mathbf{x}_t, \mathbf{x}_0) &= \frac{\|\mathcal{P}_{\mathcal{M}}^\perp \mathbf{x}_t\|^2}{2(1 - \bar{\alpha}(t))} + \frac{\|\mathcal{P}_{\mathcal{M}} \mathbf{x}_0\|^2}{2\sigma^2} + \frac{\|\mathcal{P}_{\mathcal{M}} \mathbf{x}_t - \sqrt{\bar{\alpha}(t)} \mathcal{P}_{\mathcal{M}} \mathbf{x}_0\|^2}{2(1 - \bar{\alpha}(t))} \\ &= \frac{\|\mathcal{P}_{\mathcal{M}} \mathbf{x}_0 - \boldsymbol{\mu}_t\|^2}{2s(t)} + \frac{\|\mathcal{P}_{\mathcal{M}}^\perp \mathbf{x}_t\|^2 + c(t) \|\mathcal{P}_{\mathcal{M}} \mathbf{x}_t\|^2}{2(1 - \bar{\alpha}(t))} \end{aligned}$$

and

$$s(t) = \left(\frac{1}{\sigma^2} + \frac{\bar{\alpha}(t)}{1 - \bar{\alpha}(t)}\right)^{-1} \quad (32)$$

$$\boldsymbol{\mu}_t = \frac{\frac{\sqrt{\bar{\alpha}(t)}}{1 - \bar{\alpha}(t)}}{\frac{1}{\sigma^2} + \frac{\bar{\alpha}(t)}{1 - \bar{\alpha}(t)}} \mathbf{x}_t \quad (33)$$

$$c(t) = \frac{1}{1 + \frac{\bar{\alpha}(t)}{1 - \bar{\alpha}(t)} \sigma^2} \quad (34)$$

Therefore, after integrating out with respect to \mathbf{x}_0 , we have

$$\log p(\mathbf{x}_t) = -\frac{\|\mathcal{P}_{\mathcal{M}}^\perp \mathbf{x}_t\|^2 + c(t) \|\mathcal{P}_{\mathcal{M}} \mathbf{x}_t\|^2}{2(1 - \bar{\alpha}(t))} + \text{const.}$$

leading to

$$\nabla_{\mathbf{x}_t} \log p(\mathbf{x}_t) = -\frac{1}{1 - \bar{\alpha}(t)} \mathcal{P}_{\mathcal{M}}^\perp \mathbf{x}_t - \frac{c(t)}{1 - \bar{\alpha}(t)} \mathcal{P}_{\mathcal{M}} \mathbf{x}_t$$

Furthermore, using (34), for the uniform distribution we have $\lim_{\sigma \rightarrow \infty} c(t) = 0$. Therefore,

$$\lim_{\sigma \rightarrow \infty} \nabla_{\mathbf{x}_t} \log p(\mathbf{x}_t) = -\frac{1}{1 - \bar{\alpha}(t)} \mathcal{P}_{\mathcal{M}}^\perp \mathbf{x}_t$$

Now, using Tweedie's denoising formula in (7), we have

$$\hat{\mathbf{x}}_t = \frac{1}{\sqrt{\bar{\alpha}_t}} (\mathbf{x}_t - \sqrt{1 - \bar{\alpha}_t} \boldsymbol{\epsilon}_{\theta^*}^{(t)}(\mathbf{x}_t)) \quad (35)$$

$$= \frac{1}{\sqrt{\bar{\alpha}_t}} (\mathbf{x}_t + (1 - \bar{\alpha}_t) \nabla_{\mathbf{x}_t} \log p(\mathbf{x}_t)) \quad (36)$$

where we use

$$\boldsymbol{\epsilon}_{\theta^*}^{(t)}(\mathbf{x}_t) = \nabla_{\mathbf{x}_t} \log p(\mathbf{x}_t) = -\boldsymbol{\epsilon}_{\theta^*}^{(t)}(\mathbf{x}_t) / \sqrt{1 - \bar{\alpha}_t}$$

Accordingly, we have

$$\hat{\mathbf{x}}_t = \frac{1}{\sqrt{\bar{\alpha}_t}} (\mathbf{x}_t - \mathcal{P}_{\mathcal{M}}^\perp \mathbf{x}_t) = \frac{1}{\sqrt{\bar{\alpha}_t}} \mathcal{P}_{\mathcal{M}} \mathbf{x}_t$$

and

$$\text{Denoise}(\mathbf{x}_t, \hat{\epsilon}_t) = \sqrt{\bar{\alpha}_{t-1}} \hat{\mathbf{x}}_t = \frac{\sqrt{\bar{\alpha}_{t-1}}}{\sqrt{\bar{\alpha}_t}} \mathcal{P}_{\mathcal{M}} \mathbf{x}_t$$

Similarly, we have

$$\begin{aligned} \text{Noise}(\mathbf{x}_t, \hat{\epsilon}_t) &= \sqrt{1 - \bar{\alpha}_{t-1} - \eta^2 \tilde{\beta}_t^2} \hat{\epsilon}_t \\ &= -\sqrt{1 - \bar{\alpha}_{t-1} - \eta^2 \tilde{\beta}_t^2} \sqrt{1 - \bar{\alpha}_t} \nabla_{\mathbf{x}_t} \log p(\mathbf{x}_t) \\ &= -\frac{\sqrt{1 - \bar{\alpha}_{t-1} - \eta^2 \tilde{\beta}_t^2}}{\sqrt{1 - \bar{\alpha}_t}} \mathcal{P}_{\mathcal{M}}^\perp \mathbf{x}_t \end{aligned}$$

This concludes the proof. \square

Proposition 2 (Total noise). *Assuming optimality of $\epsilon_{\theta^*}^{(t)}$, the total noise $\tilde{\mathbf{w}}_t$ in (6) can be represented by*

$$\tilde{\mathbf{w}}_t = \sqrt{1 - \bar{\alpha}_{t-1}} \tilde{\epsilon} \quad (13)$$

for some $\tilde{\epsilon} \sim \mathcal{N}(0, \mathbf{I})$. In other words, (10) is equivalently represented by $\mathbf{x}_{t-1} = \sqrt{\bar{\alpha}_{t-1}} \hat{\mathbf{x}}_t + \sqrt{1 - \bar{\alpha}_{t-1}} \tilde{\epsilon}$ for some $\tilde{\epsilon} \sim \mathcal{N}(0, \mathbf{I})$.

Proof. The proof is a direct consequence of the summation of two independent Gaussian random variables. Namely, assuming independence of $\hat{\epsilon}_t$ and ϵ , we can simply add the variance such that

$$\text{Var}(\tilde{\mathbf{w}}_t) = 1 - \bar{\alpha}_{t-1} - \eta^2 \tilde{\beta}_t^2 + \eta^2 \tilde{\beta}_t^2 = 1 - \bar{\alpha}_{t-1} \quad (37)$$

□

Proposition 3 (Concentration of noisy data). *Under Assumption 1, the probability measure $p(\mathbf{x}_{t-1})$ is concentrated on l -dimensional manifold $\mathcal{M}_{t-1} := \{\mathbf{y} \in \mathbb{R}^n : d(\mathbf{y}, \mathcal{M}) = r_{t-1} := \sqrt{(1 - \bar{\alpha}_t)(n-l)}\}$. Rigorously, $p(B_{\epsilon r_{t-1}}(\mathcal{M}_{t-1})) > 1 - \delta$, for some small $\epsilon, \delta > 0$.*

Proof. The proof borrows from and is inspired by [7]. Given the independence of the estimated $\hat{\epsilon}_t$ and the stochastic $\epsilon \sim \mathcal{N}(0, \mathbf{I})$ along with the Gaussianity, the noise variance after the update step is given as $1 - \bar{\alpha}_{t-1} - \eta^2 \tilde{\beta}_t^2 + \eta^2 \tilde{\beta}_t^2 = 1 - \bar{\alpha}_{t-1}$, recovering a sample from $q(\mathbf{x}_{t-1}|\mathbf{x}_0)$. Without loss of generality, we can equivalently define $\mathcal{M} = \{\mathbf{x} \in \mathbb{R}^d | \mathbf{x}_{l+1:d} = \mathbf{0}\}$ from linearity. Consider the forward conditional density $q(\mathbf{x}|\mathbf{x}_0) = \mathcal{N}(\sqrt{\bar{\alpha}_t} \mathbf{x}_0, (1 - \bar{\alpha}_t) \mathbf{I})$. The standard Laurent-Massart bound for chi-squared r.v. with k dof reads

$$\begin{aligned} P[X - k \geq 2\sqrt{km} + 2m] &\leq e^{-m} \\ P[X - k \leq -2\sqrt{km}] &\leq e^{-m}. \end{aligned}$$

Using the fact that $\sum_{i=l+1}^d \frac{\mathbf{x}_i^2}{1 - \bar{\alpha}_t}$ is a chi-squared r.v. with $n - l$ dof, we can substitute $m = (d - l)\epsilon'$ to get

$$\begin{aligned} P \left[-2(d-l)\sqrt{\epsilon'} \leq \sum_{i=l+1}^d \frac{\mathbf{x}_i^2}{1 - \bar{\alpha}_t} \leq 2(d-l)(\sqrt{\epsilon'} + \epsilon') \right] \\ = P \left[\sqrt{\sum_{i=l+1}^n \mathbf{x}_i^2} \in (r_t \sqrt{1 - 2\sqrt{\epsilon'}}, r_t \sqrt{1 + 2\sqrt{\epsilon'} + 2\epsilon'}) \right] \\ \geq 1 - 2e^{-(d-l)\epsilon'}. \end{aligned}$$

Finally, we have

$$\begin{aligned} p_t(\mathbf{x} \in B_{\epsilon r_t}(\mathcal{M}_t)) \\ = \int q(\mathbf{x} \in B_{\epsilon r_t}(\mathcal{M}_t) | \mathbf{x}_0) p(\mathbf{x}_0) d\mathbf{x}_0 > 1 - \delta, \end{aligned}$$

which concludes the proof. □

Lemma 1 (CG on the Clean Manifold). *For the given inverse problem (14), suppose that the clean manifold \mathcal{M} is given by the l -th order Krylov subspace \mathcal{K}_l [21], i.e.*

$$\mathcal{M} = \mathcal{K}_l = \text{Span}(\mathbf{y}, \mathbf{A}\mathbf{y}, \dots, \mathbf{A}^{l-1}\mathbf{y}) \quad (16)$$

Let $\hat{\mathbf{x}}_t^{(i)}$ denote the CG update for (14) starting with $\hat{\mathbf{x}}_t^{(0)} = \hat{\mathbf{x}}_t$. Then, we have $\hat{\mathbf{x}}_t^{(i)} \in \mathcal{M}$, $i = 1, \dots, p \leq l$.

Proof. To prove the statement, we consider the Krylov sequence $\{\hat{\mathbf{x}}_t^{(i)}\}_{i=1}^l$ for the given Krylov subspace \mathcal{K}_l , defined as

$$\hat{\mathbf{x}}_t^{(i)} = \arg \min_{\mathbf{x} \in \mathcal{K}_l} \|\mathbf{x} - \hat{\mathbf{x}}_t\|^2, \quad i = 1, \dots, l.$$

Standard results from Krylov subspace methods (see, e.g., [21]) show that the CG method generates the Krylov sequence and that by construction, each element of the sequence belongs to \mathcal{K}_l . Since we have assumed that the data manifold \mathcal{M} coincides with \mathcal{K}_l , it follows that each $\hat{\mathbf{x}}_t^{(i)}$ belongs to \mathcal{M} . Therefore, the CG method generates updated samples that lie on the data manifold \mathcal{M} , which concludes the proof. □

Theorem 1 (VP-DDS). *Suppose that $\mathcal{M} = \mathcal{K}_l$ and \mathbf{x}_t lies on the noisy manifold \mathcal{M}_t . Consider the DDS update:*

$$\mathbf{x}_{t-1} = \text{CDennoise}(\mathbf{x}_t, \hat{\epsilon}_t) + \text{Noise}(\mathbf{x}_t, \hat{\epsilon}_t) + \eta \tilde{\beta}_t \epsilon \quad (17)$$

where the function $\text{CDennoise}(\mathbf{x}_t, \hat{\epsilon}_t)$ is defined as

$$\text{CDennoise}(\mathbf{x}_t, \hat{\epsilon}_t) = \sqrt{\bar{\alpha}_{t-1}} CG^{(p)}(\hat{\mathbf{x}}_t), \quad p \leq l \quad (18)$$

and $CG^{(p)}(\hat{\mathbf{x}}_t)$ denotes the p -th CG update for (14) starting from $\hat{\mathbf{x}}_t$. Then, we can conclude that \mathbf{x}_{t-1} belongs to the noisy manifold \mathcal{M}_{t-1} .

Proof. As the CG update starting from $\hat{\mathbf{x}}_t$ always stay on the subspace $\mathcal{M} = \mathcal{K}_l$, this is a simple consequence of Lemma 1 and Proposition 2. □

Proposition 4 (VE Decomposition). *The following update rule recovers a sample from the marginal $q(\mathbf{x}_{t-1}|\mathbf{x}_0) \forall \eta \in [0, 1]$.*

$$\mathbf{x}_{t-1} = \text{Denoise}(\mathbf{x}_t, \hat{\mathbf{s}}_t) + \overbrace{\text{Noise}(\mathbf{x}_t, \hat{\mathbf{s}}_t) + \sigma_{t-1} \eta \tilde{\beta}_t \epsilon}^{\tilde{\mathbf{w}}_t} \quad (19)$$

where

$$\text{Denoise}(\mathbf{x}_t, \hat{\mathbf{s}}_t) = \hat{\mathbf{x}}_t := \mathbf{x}_t + \sigma_t^2 \hat{\mathbf{s}}_t \quad (20)$$

$$\text{Noise}(\mathbf{x}_t, \hat{\mathbf{s}}_t) = -\sigma_{t-1} \sigma_t \sqrt{1 - \tilde{\beta}^2 \eta^2} \hat{\mathbf{s}}_t \quad (21)$$

Proof. From the equivalent parameterization as in (7), we have the following relations in VE-SDE

$$\hat{\mathbf{s}}_t = -\frac{\mathbf{x}_t - \hat{\mathbf{x}}_t}{\sigma_t^2} \quad (38)$$

$$\hat{\boldsymbol{\epsilon}}_t = \frac{\mathbf{x}_t - \hat{\mathbf{x}}_t}{\sigma_t} = -\sigma_t \hat{\mathbf{s}}_t \quad (39)$$

$$\hat{\mathbf{x}}_t = \mathbf{x}_t + \sigma_t^2 \hat{\mathbf{s}}_t. \quad (40)$$

Plugging in, we have

$$\mathbf{x}_{t-1} = \hat{\mathbf{x}}_t + \sigma_{t-1} \sqrt{1 - \tilde{\beta}^2 \eta^2} \hat{\boldsymbol{\epsilon}}_t + \sigma_{t-1} \eta \tilde{\beta} \boldsymbol{\epsilon}. \quad (41)$$

Since the variance can be now computed as

$$\left(\sigma_{t-1} \sqrt{1 - \tilde{\beta}^2 \eta^2} \right)^2 + \left(\sigma_{t-1} \eta \tilde{\beta} \right)^2 = \sigma_{t-1}^2, \quad (42)$$

$\mathbf{x}_{t-1} \sim q(\mathbf{x}_{t-1}; \hat{\mathbf{x}}_t, \sigma_{t-1}^2 \mathbf{I}) = q(\mathbf{x}_{t-1} | \mathbf{x}_0)$ by the assumption. \square

Here, we present our main geometric observations in the VE context, which are analogous to Proposition 1 and Theorem 1. Their proofs are straightforward corollaries, and hence, are omitted.

Proposition 5 (VE-DDIM Decomposition). *Under Assumption 1, we have*

$$\text{Denoise}(\mathbf{x}_t, \hat{\mathbf{s}}_t) = \mathcal{P}_{\mathcal{M}} \mathbf{x}_t \quad (43)$$

$$\text{Noise}(\mathbf{x}_t, \hat{\mathbf{s}}_t) = -\sigma_{t-1} \sqrt{1 - \tilde{\beta}^2 \eta^2} \mathcal{P}_{\mathcal{M}}^\perp \mathbf{x}_t \quad (44)$$

where $\mathcal{P}_{\mathcal{M}}$ and $\mathcal{P}_{\mathcal{M}}^\perp$ denotes the orthogonal projection to the subspace \mathcal{M} and its orthogonal complement, respectively. Assuming optimality of $\mathbf{s}_{\theta^*}^{(t)}$, the total noise $\tilde{\mathbf{w}}_t$ in (19) can be represented by $\tilde{\mathbf{w}}_t = \sigma_{t-1} \tilde{\boldsymbol{\epsilon}}$ for some $\tilde{\boldsymbol{\epsilon}} \sim \mathcal{N}(0, \mathbf{I})$. In other words, (10) is then equivalently represented by $\mathbf{x}_{t-1} = \hat{\mathbf{x}}_t + \sigma_{t-1} \tilde{\boldsymbol{\epsilon}}$ for some $\tilde{\boldsymbol{\epsilon}} \sim \mathcal{N}(0, \mathbf{I})$.

Accordingly, we can obtain the following key result for

Theorem 2 (VE-DDS). *Suppose that $\mathcal{M} = \mathcal{K}_l$ and \mathbf{x}_t lies on the noisy manifold \mathcal{M}_t . Consider the DDS update:*

$$\mathbf{x}_{t-1} = \text{CDenoise}(\mathbf{x}_t, \hat{\boldsymbol{\epsilon}}_t) + \text{Noise}(\mathbf{x}_t, \hat{\boldsymbol{\epsilon}}_t) + \eta \tilde{\beta} \boldsymbol{\epsilon} \quad (45)$$

where the function $\text{CDenoise}(\mathbf{x}_t, \hat{\boldsymbol{\epsilon}}_t)$ is defined as

$$\text{CDenoise}(\mathbf{x}_t, \hat{\boldsymbol{\epsilon}}_t) = CG^{(p)}(\hat{\mathbf{x}}_t), \quad p \leq l \quad (46)$$

and $CG^{(p)}(\hat{\mathbf{x}}_t)$ denotes the p -th CG update for (14) starting from $\hat{\mathbf{x}}_t$. Then, we can conclude that \mathbf{x}_{t-1} belongs to the noisy manifold \mathcal{M}_{t-1} .

Algorithm 1 DDS (PI MRI; VP; noiseless)

Require: $\boldsymbol{\epsilon}_{\theta^*}, N, \{\alpha_t\}_{t=1}^N, \eta, \mathbf{A}, M$

```

1:  $\mathbf{x}_N \sim \mathcal{N}(\mathbf{0}, \mathbf{I})$ 
2: for  $t = N : 2$  do
3:    $\hat{\boldsymbol{\epsilon}}_t \leftarrow \boldsymbol{\epsilon}_{\theta^*}(\mathbf{x}_t)$ 
4:    $\triangleright$  Tweedie denoising
5:    $\hat{\mathbf{x}}_t \leftarrow (\mathbf{x}_t - \sqrt{1 - \bar{\alpha}_t} \hat{\boldsymbol{\epsilon}}_t) / \sqrt{\bar{\alpha}_t}$ 
6:    $\triangleright$  Data consistency
7:    $\hat{\mathbf{x}}'_t \leftarrow \text{CG}(\mathbf{A}^* \mathbf{A}, \mathbf{A}^* \mathbf{y}, \hat{\mathbf{x}}_t, M)$ 
8:    $\boldsymbol{\epsilon} \sim \mathcal{N}(\mathbf{0}, \mathbf{I})$ 
9:    $\triangleright$  DDIM sampling
10:   $\mathbf{x}_{t-1} \leftarrow \sqrt{\bar{\alpha}_{t-1}} \hat{\mathbf{x}}'_t - \sqrt{1 - \bar{\alpha}_{t-1} - \eta^2 \tilde{\beta}_t^2} \hat{\boldsymbol{\epsilon}}_t + \eta \tilde{\beta}_t \boldsymbol{\epsilon}$ 
11: end for
12:  $\mathbf{x}_0 \leftarrow (\mathbf{x}_1 - \sqrt{1 - \bar{\alpha}_1} \boldsymbol{\epsilon}_{\theta^*}(\mathbf{x}_1)) / \sqrt{\bar{\alpha}_1}$ 
13: return  $\mathbf{x}_0$ 
```

Algorithm 2 DDS (PI MRI; VP; noisy)

Require: $\boldsymbol{\epsilon}_{\theta^*}, N, \{\alpha_t\}_{t=1}^N, \eta, \mathbf{A}, M, \gamma$

```

1:  $\mathbf{x}_N \sim \mathcal{N}(\mathbf{0}, \mathbf{I})$ 
2: for  $t = N : 2$  do
3:    $\hat{\boldsymbol{\epsilon}}_t \leftarrow \boldsymbol{\epsilon}_{\theta^*}(\mathbf{x}_t)$ 
4:    $\triangleright$  Tweedie denoising
5:    $\hat{\mathbf{x}}_t \leftarrow (\mathbf{x}_t - \sqrt{1 - \bar{\alpha}_t} \hat{\boldsymbol{\epsilon}}_t) / \sqrt{\bar{\alpha}_t}$ 
6:    $\triangleright$  Data consistency
7:    $\mathbf{A}_{\text{CG}} \leftarrow \mathbf{I} + \gamma \mathbf{A}^* \mathbf{A}$ 
8:    $\mathbf{y}_{\text{CG}} \leftarrow \hat{\mathbf{x}}_t + \gamma \mathbf{A}^* \mathbf{y}$ 
9:    $\hat{\mathbf{x}}'_t \leftarrow \text{CG}(\mathbf{A}_{\text{CG}}, \mathbf{y}_{\text{CG}}, \hat{\mathbf{x}}_t, M)$ 
10:   $\boldsymbol{\epsilon} \sim \mathcal{N}(\mathbf{0}, \mathbf{I})$ 
11:   $\triangleright$  DDIM sampling
12:   $\mathbf{x}_{t-1} \leftarrow \sqrt{\bar{\alpha}_{t-1}} \hat{\mathbf{x}}'_t - \sqrt{1 - \bar{\alpha}_{t-1} - \eta^2 \tilde{\beta}_t^2} \hat{\boldsymbol{\epsilon}}_t + \eta \tilde{\beta}_t \boldsymbol{\epsilon}$ 
13: end for
14:  $\mathbf{x}_0 \leftarrow (\mathbf{x}_1 - \sqrt{1 - \bar{\alpha}_1} \boldsymbol{\epsilon}_{\theta^*}(\mathbf{x}_1)) / \sqrt{\bar{\alpha}_1}$ 
15: return  $\mathbf{x}_0$ 
```

B. Algorithms

We list all the DDS algorithms used throughout the manuscript. For simplicity, we define $\text{CG}(\mathbf{A}, \mathbf{y}, \mathbf{x}, M)$ to be running M steps of conjugate gradient steps with initialization \mathbf{x} .

C. Discussion on Conditioning

Projection type Methods that belong to this class aim to directly replace³ what we have in the *range space* of the intermediate noisy \mathbf{x}_i with the information from the measurement \mathbf{y} . Two representative works that utilize projection are [9] and [33]. In [9], we use

$$\mathbf{x}_t = (\mathbf{I} - \mathbf{A}^\dagger \mathbf{A}) \mathbf{x}'_t + \mathbf{A}^\dagger \mathbf{y}, \quad (47)$$

³Both hard [9] or soft [33] constraints can be utilized.

Algorithm 3 DDS (3D CT recon; VP)

Require: $\epsilon_{\theta^*}, N, \{\sigma_t\}_{t=1}^N, \eta, \mathbf{A}, M, \{\lambda_t\}_{t=1}^N$

- 1: $\mathbf{x}_N \sim \mathcal{N}(\mathbf{0}, \sigma_T^2 \mathbf{I})$
- 2: $\mathbf{z}_N \leftarrow \text{torch.zeros_like}(\mathbf{x}_N)$
- 3: $\mathbf{w}_N \leftarrow \text{torch.zeros_like}(\mathbf{x}_N)$
- 4: **for** $i = N : 2$ **do**
- 5: $\hat{\epsilon}_t \leftarrow \epsilon_{\theta^*}(\mathbf{x}_t)$
- 6: ▷ Tweedie denoising
- 7: $\hat{\mathbf{x}}_t \leftarrow (\mathbf{x}_t - \sqrt{1 - \bar{\alpha}_t} \hat{\epsilon}_t) / \sqrt{\bar{\alpha}_t}$
- 8: ▷ Data consistency
- 9: $\mathbf{A}_{\text{CG}} \leftarrow \mathbf{A}^T \mathbf{A} + \rho \mathbf{D}_z^T \mathbf{D}_z$
- 10: $\mathbf{b}_{\text{CG}} \leftarrow \mathbf{A}^T \mathbf{y} + \rho \mathbf{D}_z^T (\mathbf{z}_{t+1} - \mathbf{w}_{t+1})$
- 11: $\hat{\mathbf{x}}'_t \leftarrow \text{CG}(\mathbf{A}_{\text{CG}}, \mathbf{b}_{\text{CG}}, \hat{\mathbf{x}}_t, M)$
- 12: $\mathbf{z}_t \leftarrow \mathcal{S}_{\lambda_t/\rho}(\mathbf{D}_z \hat{\mathbf{x}}'_t + \mathbf{w}_{t+1})$
- 13: $\mathbf{w}_t \leftarrow \mathbf{w}_{t+1} + \mathbf{D}_z \hat{\mathbf{x}}'_t - \mathbf{z}_t$
- 14: ▷ DDIM sampling
- 15: $\mathbf{x}_{t-1} \leftarrow \sqrt{\bar{\alpha}_{t-1}} \hat{\mathbf{x}}'_t - \sqrt{1 - \bar{\alpha}_{t-1} - \eta^2 \bar{\beta}_t^2} \hat{\epsilon}_t + \eta \bar{\beta}_t \epsilon$
- 16: **end for**
- 17: $\mathbf{x}_0 \leftarrow (\mathbf{x}_1 - \sqrt{1 - \bar{\alpha}_1} \epsilon_{\theta^*}(\mathbf{x}_1)) / \sqrt{\bar{\alpha}_1}$

Algorithm 4 DDS (PI MRI; VE)

Require: $s_{\theta^*}, N, \{\sigma_t\}_{t=1}^N, \eta, \mathbf{A}, M$

- 1: $\mathbf{x}_N \sim \mathcal{N}(\mathbf{0}, \sigma_T^2 \mathbf{I})$
- 2: **for** $t = N : 2$ **do**
- 3: $\hat{s}_t \leftarrow s_{\theta^*}(\mathbf{x}_t)$
- 4: ▷ Tweedie denoising
- 5: $\hat{\mathbf{x}}_t \leftarrow \mathbf{x}_t + \sigma_t^2 s_{\theta^*}(\mathbf{x}_t)$
- 6: ▷ Data consistency
- 7: $\hat{\mathbf{x}}'_t \leftarrow \text{CG}(\mathbf{A}^* \mathbf{A}, \mathbf{A}^* \mathbf{y}, \hat{\mathbf{x}}_t, M)$
- 8: $\epsilon \sim \mathcal{N}(\mathbf{0}, \mathbf{I})$
- 9: ▷ DDIM sampling
- 10: $\mathbf{x}_{t-1} \leftarrow \hat{\mathbf{x}}'_t - \sigma_{t-1}^2 \sqrt{1 - \eta^2} \hat{s}_t + \sigma_{t-1} \epsilon$
- 11: **end for**
- 12: $\mathbf{x}_0 \leftarrow \mathbf{x}_1 + \sigma_1^2 s_{\theta^*}(\mathbf{x}_1)$
- 13: **return** \mathbf{x}_0

where the information from \mathbf{y} will be used to fill in the range space of \mathbf{A}^\dagger . However, this is clearly problematic when considering the geometric viewpoint, as the sample may fall off the noisy manifold.

Gradient type In the Bayesian reconstruction perspective, it is natural to incorporate the gradient of the likelihood as $\nabla \log p(\mathbf{x}_t | \mathbf{y}) = \nabla \log p(\mathbf{x}_t) + \nabla \log p(\mathbf{y} | \mathbf{x}_t)$. Here, while one can use $\nabla \log p(\mathbf{x}_t) \simeq s_{\theta^*}(\mathbf{x}_t)$, $\nabla \log p(\mathbf{y} | \mathbf{x}_t)$ is intractable for all $t \neq 0$ [5], one has to resort to approximations of $\nabla \log p(\mathbf{y} | \mathbf{x}_t)$. In a similar spirit to Score-MRI [9], one can simply use gradient steps of the form

$$\mathbf{x}_t = \mathbf{x}'_t - \xi_t \mathbf{A}^* (\mathbf{y} - \mathbf{A} \mathbf{x}'_t), \quad (48)$$

where ξ_t is the step size [15]. Nevertheless, $\nabla_{\mathbf{x}_t} \log p(\mathbf{x}_t | \mathbf{y})$ is far from Gaussian as i gets further away from 0, and hence is hard to interpret nor analyze what the gradient steps in the direction of $\mathbf{A}^* (\mathbf{y} - \mathbf{A} \mathbf{x}'_t)$ is leading. Albeit not in the context of MRI, a more recent approach [5] proposes to use

$$\mathbf{x}_t = \mathbf{x}'_t - \xi_t \nabla_{\mathbf{x}_{t+1}} \|\mathbf{y} - \mathbf{A} \hat{\mathbf{x}}_{t+1}\|_2^2. \quad (49)$$

As $\hat{\mathbf{x}}_{t+1}$ is the Tweedie denoised estimate and is free from Gaussian noise, (49) can be thought of as minimizing the residual *on the noiseless data manifold* \mathcal{M} . However, care must be taken since taking the gradient with respect to \mathbf{x}_t corresponds to computing automatic differentiation through the neural net s_{θ^*} , often slowing down the compute by about $\times 2$ [5].

T2I vs. DIS For the former, the likelihood is usually given as a neural net-parameterized function $p_\phi(\mathbf{y} | \mathbf{x})$ (e.g. classifier, implicit gradient from CFG), whereas for the latter, the likelihood is given as an analytic distribution arising from some linear/non-linear forward operator [18, 5].

D. Algorithmic details

We provide the VP counterpart of the DDS VE algorithms presented in Algorithm 4,5 in Algorithm 1,3. The only differences are that the model is now parameterized with ϵ_θ that estimates the residual noise components, and that we have a different noise schedule.

D.1. Accelerated MRI

As stated in §4.1, using ≥ 200 NFE when using Algorithm 4 degrades the performance due to the numerical instability. To counteract this issue, we use the same iteration until $i \leq N/50 =: k$, and directly acquire the final reconstruction by the Tweedie’s formula:

$$\mathbf{x}_0 = \mathbf{x}_k + \sigma_k^2 s_{\theta^*}(\mathbf{x}_k) \quad (50)$$

D.2. 3D CT reconstruction

Recall that in order to perform 3D reconstruction, we resort to the following optimization problem (omitting the indices for simplicity)

$$\hat{\mathbf{x}}^* = \arg \min_{\hat{\mathbf{x}}} \frac{1}{2} \|\mathbf{A} \hat{\mathbf{x}} - \mathbf{y}\|_2^2 + \lambda \|\mathbf{D}_z \hat{\mathbf{x}}\|_1. \quad (51)$$

One can utilize ADMM to stably solve the above problem. Here, we include the steps to arrive at Algorithms 5,3 for completeness. Reformulating into a constrained optimization problem, we have

$$\min_{\mathbf{x}, \mathbf{z}} \frac{1}{2} \|\mathbf{y} - \mathbf{A} \hat{\mathbf{x}}\|_2^2 + \lambda \|\mathbf{z}\|_1 \quad (52)$$

$$\text{s.t. } \mathbf{z} = \mathbf{D}_z \hat{\mathbf{x}}. \quad (53)$$

Then, ADMM can be implemented as separate update steps for the primal and the dual variables

$$\hat{\mathbf{x}}_{j+1} = \arg \min_{\hat{\mathbf{x}}_j} \frac{1}{2} \|\mathbf{y} - \mathbf{A}\hat{\mathbf{x}}_j\|_2^2 + \frac{\rho}{2} \|\mathbf{D}_z \hat{\mathbf{x}}_j - \mathbf{z}_j + \mathbf{w}\|_2^2 \quad (54)$$

$$\mathbf{z}_{j+1} = \arg \min_{\mathbf{z}_j} \lambda \|\mathbf{z}_j\|_1 + \frac{\rho}{2} \|\mathbf{D}_z \hat{\mathbf{x}}_j - \mathbf{z}_j + \mathbf{w}\|_2^2 \quad (55)$$

$$\mathbf{w}_{j+1} = \mathbf{w}_j + \mathbf{D}_z \hat{\mathbf{x}}_{j+1} - \mathbf{z}_{j+1}. \quad (56)$$

We have a closed-form solution for (54)

$$\hat{\mathbf{x}}_{j+1} = (\mathbf{A}^T \mathbf{A} + \rho \mathbf{D}_z^T \mathbf{D}_z)^{-1} (\mathbf{A}^T \mathbf{y} + \rho \mathbf{D}_z^T (\mathbf{z} - \mathbf{w})), \quad (57)$$

which can be numerically solved by iterative CG

$$\hat{\mathbf{x}}_{j+1} = \text{CG}(\mathbf{A}_{\text{CG}}, \mathbf{b}_{\text{CG}}, \hat{\mathbf{x}}_j, M) \quad (58)$$

$$\mathbf{A}_{\text{CG}} := \mathbf{A}^T \mathbf{A} + \rho \mathbf{D}_z^T \mathbf{D}_z \quad (59)$$

$$\mathbf{b}_{\text{CG}} := \mathbf{A}^T \mathbf{y} + \rho \mathbf{D}_z^T (\mathbf{z} - \mathbf{w}). \quad (60)$$

Moreover, as (55) is in the form of proximal mapping [26], we have that

$$\mathbf{z}_{j+1} = \mathcal{S}_{\lambda/\rho}(\mathbf{D}_z \mathbf{x} + \mathbf{w}). \quad (61)$$

Thus, we have the following update steps

$$\begin{aligned} \hat{\mathbf{x}}_{j+1} &= \text{CG}(\mathbf{A}_{\text{CG}}, \mathbf{b}_{\text{CG}}, \hat{\mathbf{x}}_j, M) \\ \mathbf{z}_{j+1} &= \mathcal{S}_{\lambda/\rho}(\mathbf{D}_z \hat{\mathbf{x}}_{j+1} + \mathbf{w}_j) \\ \mathbf{w}_{j+1} &= \mathbf{w}_j + \mathbf{D}_z \hat{\mathbf{x}}_{j+1} - \mathbf{z}_{j+1}. \end{aligned}$$

Usually, such update step is performed in an iterative fashion until convergence. However, in our algorithm for 3D reconstruction (Algorithm 5, 3), we only use a single iteration of ADMM per each step of denoising. This is possible as we share the primal variable \mathbf{z} and the dual variable \mathbf{w} as global variables throughout the update steps, leading to proper convergence with a single iteration (fast variable sharing technique [6]).

Stabilizing Algorithm 5 As stated in §4.2, in order to stabilize Algorithm 5, we found it beneficial to first start the DC imposing strategy with simple CG update steps without TV prior, as used in our MRI experiments. We iterate our solver starting from $i = N$ down to $N/2$ using standard CG updates. Then, we switch to ADMM-TV scheme starting from $i = N/2 - 1$ down to 2.

E. Additional Experiments

E.1. Noise offset

For this experiment, we take 50 random proton density (PD) weighted images from the fastMRI validation dataset,

Method	No process	Score-MRI [9]	Jalal <i>et al.</i> [15]	DPS [5]	DDNM [37]	DDS (CG)
σ_{est}	7.556	5.959	6.303	8.527	8.256	7.859
$ \sigma_{\text{est}}^{\text{np}} - \sigma_{\text{est}} $	0.000	1.597	1.253	0.917	0.700	0.303

Table E.1: Noise offset experiment. Gaussian noise level estimated with [4]. Real noise level: $\sigma_{\text{GT}} = 7.00[\times 10^{-2}]$; $\sigma_{\text{est}}^{\text{np}} = 7.56[\times 10^{-2}]$

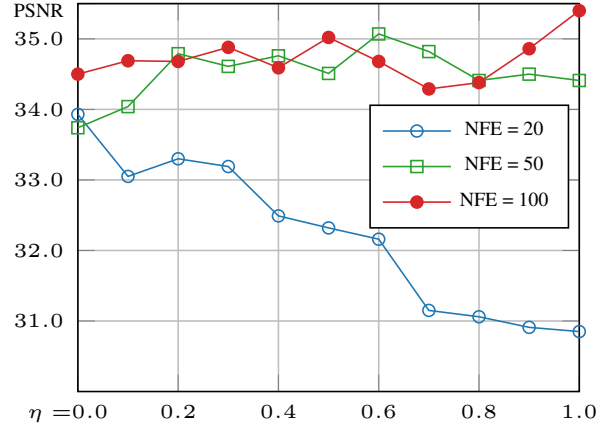


Figure E.1: Ablation study on the selection of η for Algorithm 1.

and add Gaussian noise $\sigma_{\text{GT}} = 7.00[\times 10^{-2}]$ to the images. For each noisy image, we apply the following DC step for each method

1. Score-MRI [9]: (47)
2. Jalal *et al.* [15]: (48) with step size as used in the implementation⁴
3. DPS [5]: (49) with step size 1.0
4. DDNM [37]: (25)
5. DDS (CG): CG applied to the Tweedie denoised estimate, $M = 5$.

Once the update step is performed, Gaussian noise level of the updated samples are estimated with the method from [4]. Note that as the estimation method is imperfect, there is already a gap between the ground truth noise level and the estimated noise level.

E.2. Stochasticity in sampling

For our sampling strategy, the stochasticity of the sampling process is determined by the parameter $\eta \in [0, 1]$. When $\eta \rightarrow 0$, the sampling becomes deterministic, whereas

⁴<https://github.com/utcsilab/csgm-mri-langevin/blob/main/main.py>

when $\eta \rightarrow 1$, the sampling becomes maximally stochastic. It is known in the literature that for unconditional sampling using low NFE, setting η as close to 0 leads to better performance [30]. In Fig. E.1, we see a similar trend when we set NFE = 20. However, when we set NFE ≥ 50 , we observe that the choice of η does not matter too much, as it often fluctuates within the boundary that can be as well be thought of as arising from the inherent stochasticity of the sampling procedure. This is different from the observation made in [30], which can be thought of as stemming from the conditional sampling strategy that the proposed method uses.

E.3. Instability in VE parameterization

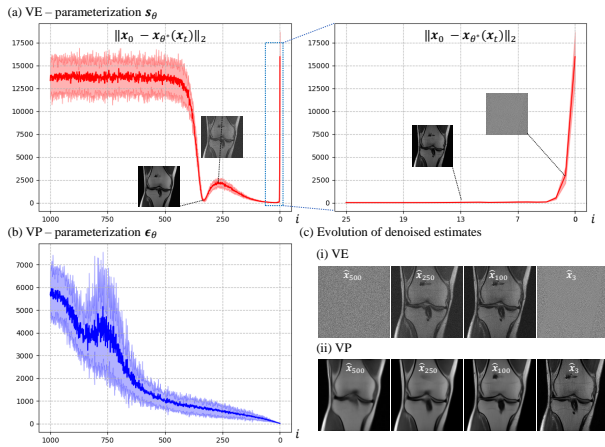


Figure E.2: Evolution of the reconstruction error through time. $\pm 1.0\sigma$ plot. (a) VE parameterized with s_θ , (b) VP parameterized with ϵ_θ , (c) Visualization of \hat{x}_t .

NFE	4000	500	200	100	50	30
Score-MRI [9]	33.25	33.19	33.13	31.67	3.015	3.239
Ours	32.07	31.16	31.99	33.69	31.79	30.40

Table E.2: PSNR [db] of uniform 1D $\times 4$ acc. reconstruction with varying NFEs. Numbers in red: failure cases.

One observation that is made in this experiment, however, is that using ≥ 200 NFEs for the proposed method actually *degrades* the performance. We find that this degradation stems from the numerical pathologies that arise when VE-SDE is combined with the parameterizing the neural network with s_θ . Specifically, the score function is parameterized to estimate $s_{\theta^*}(x_t) \simeq -\frac{x_t - x_0}{\sigma_t^2} = \epsilon/\sigma_t$. Near $t = 0$, σ_t attains a very small value *e.g.* $\sigma_0 = 0.01$ [19], meaning that the score function has to approximate relatively large values in such regime, leading to numerical instability. This phenomenon is further illustrated in Fig. E.2 (a), where the

Method	Axial*		Coronal		Sagittal	
	PSNR \uparrow	SSIM \uparrow	PSNR \uparrow	SSIM \uparrow	PSNR \uparrow	SSIM \uparrow
DDS VP (49)	35.07	0.963	32.90	0.955	29.34	0.861
DiffusionMBIR [6]	34.92	0.956	32.48	0.947	28.82	0.832
Chung <i>et al.</i> [7]	26.01	0.838	24.55	0.823	21.59	0.706
Lahiri <i>et al.</i> [20]	28.08	0.931	26.02	0.856	23.24	0.812
Zhang <i>et al.</i> [40]	26.76	0.879	25.77	0.874	22.92	0.841
ADMM-TV	23.19	0.793	22.96	0.758	19.95	0.782

Table E.3: Quantitative evaluation of LA-CT (90°) on the AAPM 256×256 test set. **Bold:** Best.

reconstruction (i.e. denoising) error has a rather odd trend of jumping up and down, and completely diverging as $t \rightarrow 0$. This may be less of an issue for using samplers such as PC where \hat{x}_i are not directly used, but becomes a much bigger problem when the proposed sampler is used. In fact, for NFE > 200 , we find that simply truncating the last few evolutions is necessary to yield the result reported in Tab. E.2 (See appendix D.1 for details).

Such instabilities worsen when we tried scaling our experiments to complex-valued PI reconstruction due to the network only being trained on magnitude images. On the other hand, the reconstruction errors for VP trained with epsilon matching have a much stabler evolution of denoising reconstructions, suggesting that it is indeed a better fit in the context of the proposed methodology. Hence, all experiments reported hereafter uses a network parameterized with ϵ_θ trained within a VP framework, and also by stacking real/imag part in the channel dimension to account for the complex-valued nature of the MR imagery, and to avoid using $\times 2$ NFE for a single level of denoising.

F. Experimental Details

F.1. Datasets

fastMRI knee. We conduct all PI experiments with fastMRI knee dataset [39]. Following the practices from [9], among the 973 volumes of training data, we drop the first/last five slices from each volume. As the test set, we select 10 volumes from the validation dataset. While [8] used DICOM magnitude images to train the network, we used the minimum-variance unbiased estimates (MVUE) [15] complex-valued data by stacking the real and imaginary parts of the images into the channel dimension. When performing inference, we pre-compute the coil sensitivity maps with ESPiRiT [36].

AAPM. AAPM 2016 CT low-dose grand challenge data leveraged in [7, 6] is used. From the filtered backprojection (FBP) reconstruction of size 512×512 , we resize all the images to have the size 256×256 in the axial dimension. We use the same 1 volume of testing data that was used in [6]. To generate sparse-view and limited angle measurements, we use the parallel view geometry for simplicity, with the `torch-radon` [27] package.

F.2. Network training

VE models for both MRI/CT are taken from the official github repositories [9, 7], which are both based on `nscsnpp` model of Score-SDE [34]. In order to train our VP epsilon matching models, we take the U-Net implementation from ADM [10], and train each model for 1M iterations with the batch size of 4, initial learning rate of $1e - 4$ on a single RTX 3090 GPU. Training took about 3 days for each task.

Code availability We will fully open-source our code and pretrained models to reproduce all experiments in the paper upon publication.

F.3. Rejection sampling

When running Algorithm 1 in the low NFE regime (e.g. 19, 49), we see that our method sometimes yields infeasible reconstructions. Sampling 100 reconstructions for 1D uniform $\times 4$ acc., we see that 5% of the samples were infeasible for 19 NFE, and 3% of the samples were infeasible for 49 NFE. In such cases, we simply compute the Euclidean norm of the residual $\|\mathbf{y} - \mathbf{A}\hat{\mathbf{x}}\|$ with the reconstructed sample $\hat{\mathbf{x}}$, and reject the sample if the residual exceeds some threshold value τ . Even when we consider the additional time costs that arise from re-sampling the rejected reconstructions, we still achieve dramatic acceleration to previous methods [33, 9].

F.4. Comparison methods

F.4.1 Accelerated MRI

Score-MRI [9] We use the official pre-trained model⁵ with 2000 PC sampling. Note that for PI, this amounts to running the sampling procedure per coil. When reducing the number of NFE presented in Fig. 1, we use linear discretization with wider bins.

Jalal *et al.* [15]. As the official pre-trained model is trained on fastMRI brain MVUE images, in order to perform fair comparison, we train the NCSN v2 model with the same fastMRI knee MVUE images for 1M iterations in the setting identical to when training the model for the proposed method. For inference, we follow the default annealing step sizes as proposed in the original paper. We use 3 Langevin dynamics steps per noise scale for 700 discretizations, which amounts to a total of 2100 NFE. When reducing the number of NFE presented in Fig. 1, we keep the 3 Langevin steps intact, and use linear discretization with wider bins.

E2E-Varnet [35], U-Net. We train the supervised learning-based methods with Gaussian 1D subsampling as performed in [9], adhering to the official implementation and the default settings of the original work.

⁵<https://github.com/HJ-harry/score-MRI>

TV. We use the implementation in `siggy.mri.app.TotalVariation`⁶, with calibrated sensitivity maps with ESPiRiT [36]. The parameters for the optimizer are found via grid search on 50 validation images.

F.4.2 3D CT reconstruction

DiffusionMBIR [6], Chung *et al.* [7]. Both methods use the same score function as provided in the official repository⁷. For both DiffusionMBIR and Score-CT, we use 2000 PC sampler (4000 NFE). For DiffusionMBIR, we set $\lambda = 10.0, \rho = 0.04$, which is the advised parameter setting for the AAPM 256 \times 256 dataset. For Chung *et al.*, we use the iterating ART projections as used in the comparison study in [6].

Lahiri *et al.* [20]. We use two stages of 3D U-Net based CNN architectures. For each greedy optimization process, we train the network for 300 epochs. For CG, we use 30 iterations at each stage. Networks were trained with the Adam optimizer with a static learning rate of $1e - 4$, batch size of 2.

FBPConvNet [16], Zhang *et al.* [40]. Both methods utilize the same network architecture and the same training strategy, only differing in the application (SV, LA). We use a standard 2D U-Net architecture and train the models with 300 epochs. Networks were trained with the Adam optimizer with a learning rate of $1e - 4$, batch size 8.

ADMM-TV. Following the protocol of [6], we optimize the following objective

$$\mathbf{x}^* = \arg \min_{\mathbf{x}} \frac{1}{2} \|\mathbf{A}\mathbf{x} - \mathbf{y}\|_2^2 + \lambda \|\mathbf{D}\mathbf{x}\|_{2,1}, \quad (62)$$

with $\mathbf{D} := [\mathbf{D}_x, \mathbf{D}_y, \mathbf{D}_z]$, and is solved with standard ADMM and CG. Hyper-parameters are set identical to [6].

G. Qualitative results

⁶<https://github.com/mikgroup/siggy>

⁷<https://github.com/HJ-harry/MCG-diffusion>

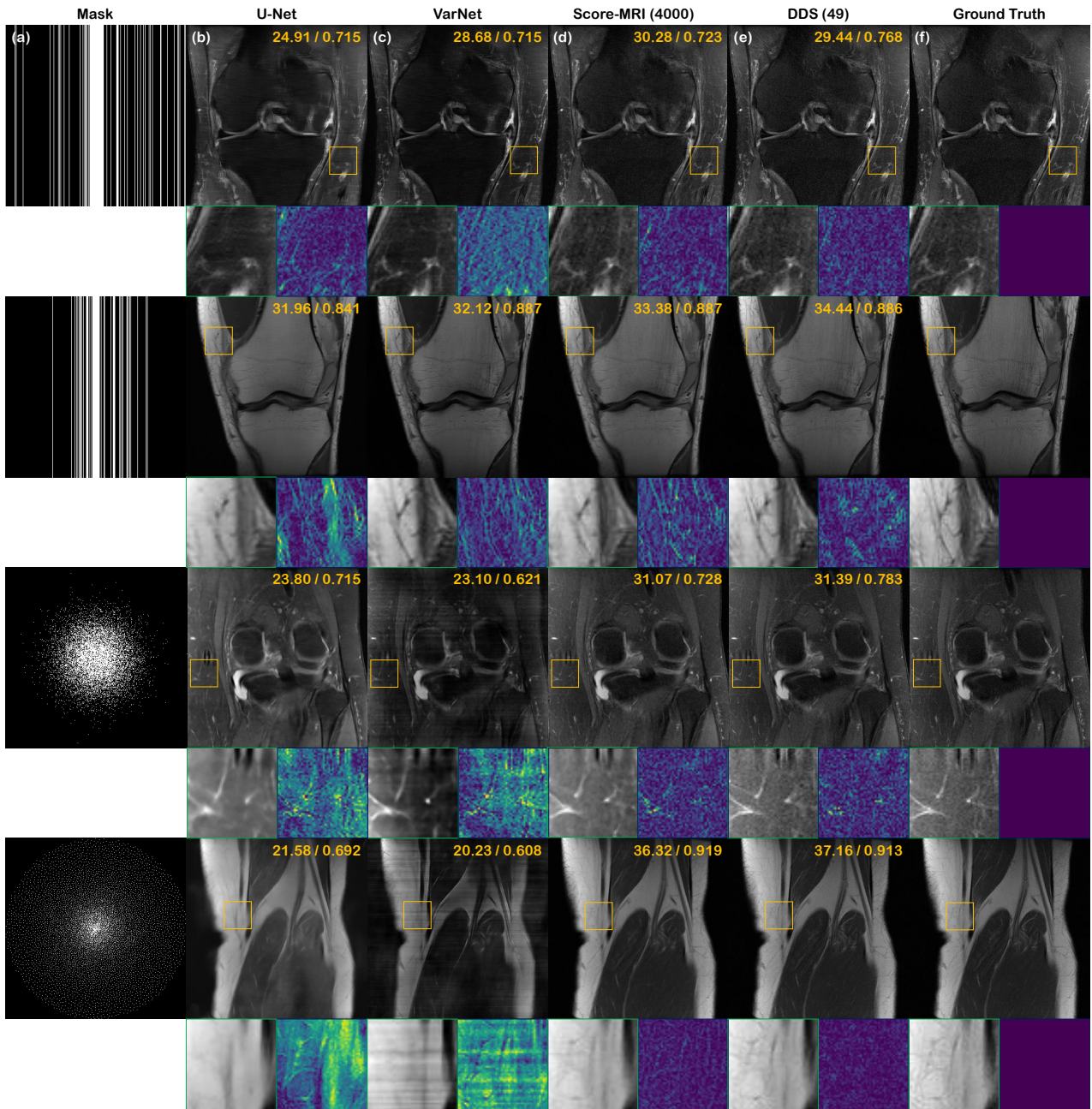


Figure G.1: Comparison of parallel imaging reconstruction results. (a) subsampling mask (1st row: uniform 1D \times 4, 2nd row: gaussian 1D \times 8, 3rd row: gaussian 2D \times 8, 4th row: variable density poisson disc \times 8), (b) U-Net [39], (c) E2E-VarNet [35], (d) Score-MRI [9] (4000 \times 2 \times c NFE), (e) DDS (49 NFE), (f) ground truth.

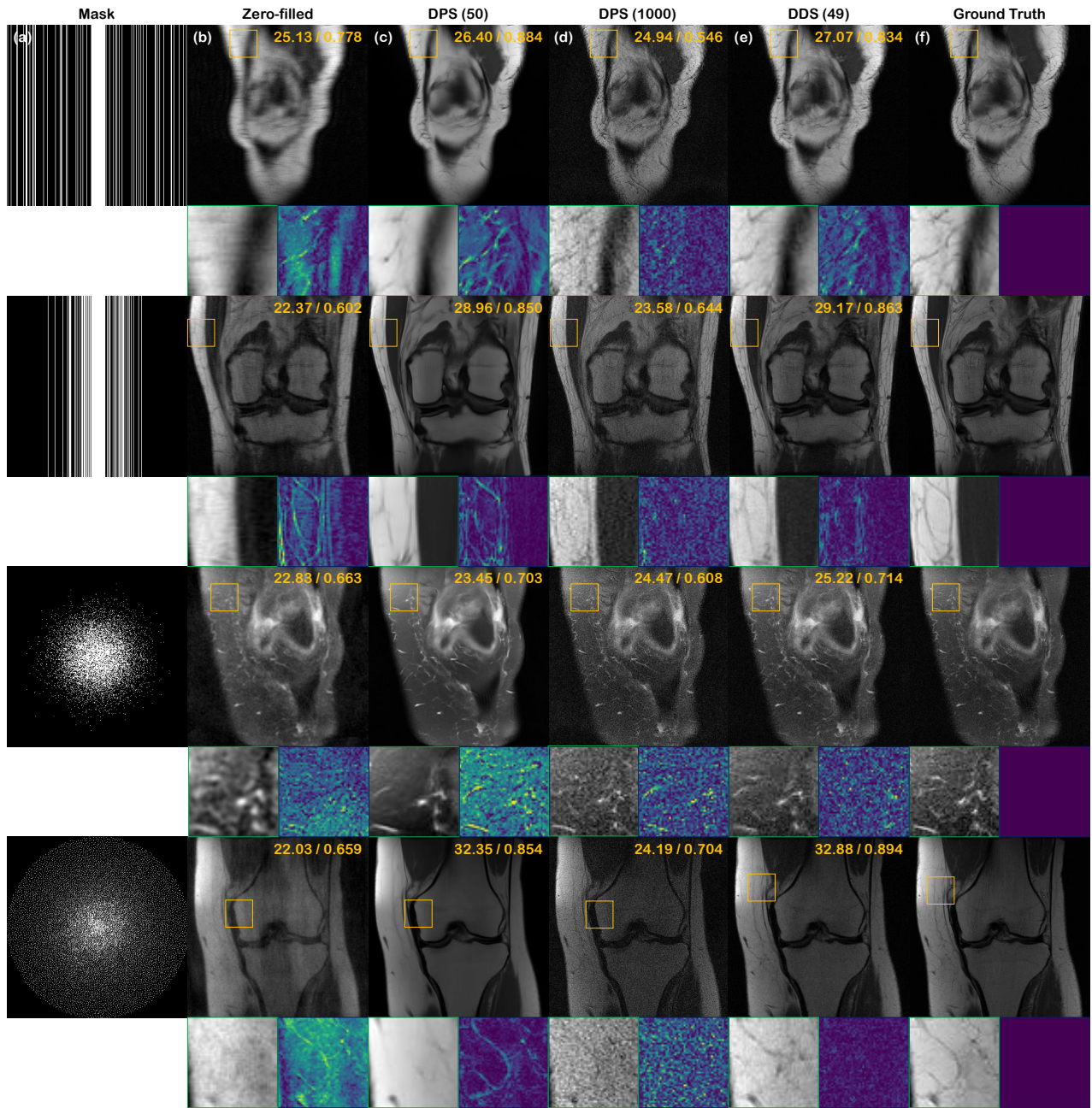


Figure G.2: Comparison of noisy ($\sigma = 0.05$) parallel imaging reconstruction results. (a) subsampling mask (1st row: uniform $1D \times 4$, 2nd row: gaussian $1D \times 4$, 3rd row: gaussian $2D \times 8$, 4th row: variable density poisson disc $\times 8$), (b) Zero-filled, (c) DPS [5] (50 NFE), (d) DPS [5] (1000 NFE), (e) DDS (49 NFE), (f) ground truth. Numbers in the top right corners denote PSNR and SSIM, respectively.

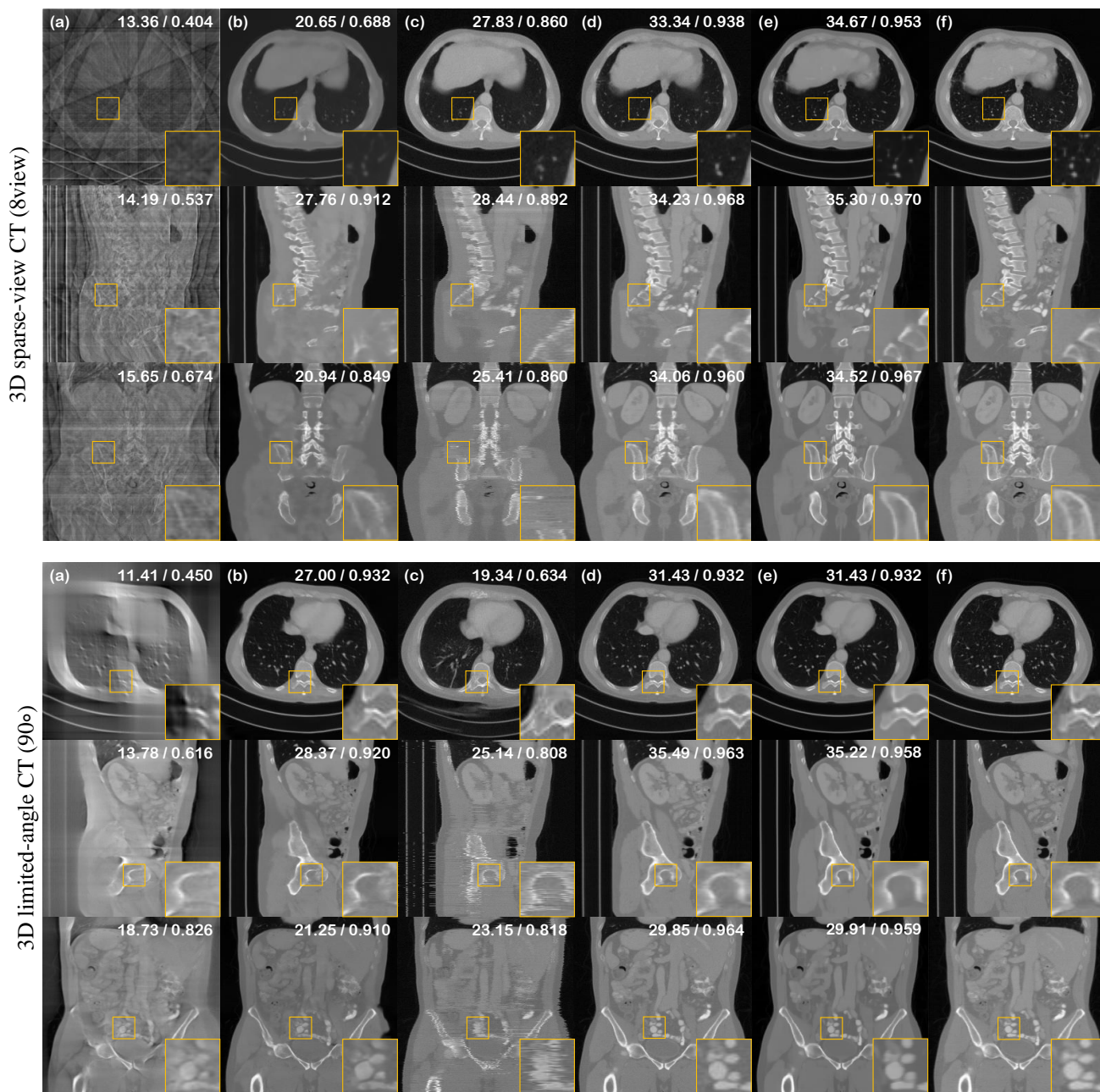


Figure G.3: Comparison of 3D CT reconstruction results. (**Top**): 8-view SV-CT, (**Bottom**): 90° LA-CT. (a) FBP, (b) Lahiri *et al.*, (c) Chung *et al.*, (d) DiffusionMBIR (4000 NFE), (e) DDS (49 NFE), (f) ground truth. Numbers in top right corners denote PSNR and SSIM, respectively.

Algorithm 5 DDS (3D CT recon; VE)

Require: $s_{\theta^*}, N, \{\sigma_t\}_{t=1}^N, \eta, \mathbf{A}, M, \{\lambda_t\}_{t=1}^N$

- 1: $\mathbf{x}_N \sim \mathcal{N}(\mathbf{0}, \sigma_T^2 \mathbf{I})$
 - 2: $\mathbf{z}_N \leftarrow \text{torch.zeros_like}(\mathbf{x}_N)$
 - 3: $\mathbf{w}_N \leftarrow \text{torch.zeros_like}(\mathbf{x}_N)$
 - 4: **for** $t = N : 2$ **do**
 - 5: $\hat{\mathbf{s}}_t \leftarrow s_{\theta^*}(\mathbf{x}_t)$
 - 6: \triangleright Tweedie denoising
 - 7: $\hat{\mathbf{x}}_t \leftarrow \mathbf{x}_t + \sigma_t^2 s_{\theta^*}(\mathbf{x}_t)$
 - 8: \triangleright Data consistency
 - 9: $\mathbf{A}_{\text{CG}} \leftarrow \mathbf{A}^T \mathbf{A} + \rho \mathbf{D}_z^T \mathbf{D}_z$
 - 10: $\mathbf{b}_{\text{CG}} \leftarrow \mathbf{A}^T \mathbf{y} + \rho \mathbf{D}_z^T (\mathbf{z}_{t+1} - \mathbf{w}_{t+1})$
 - 11: $\hat{\mathbf{x}}'_t \leftarrow \text{CG}(\mathbf{A}_{\text{CG}}, \mathbf{b}_{\text{CG}}, \hat{\mathbf{x}}_t, M)$
 - 12: $\mathbf{z}_t \leftarrow \mathcal{S}_{\lambda_t/\rho}(\mathbf{D}_z \hat{\mathbf{x}}'_t + \mathbf{w}_{t+1})$
 - 13: $\mathbf{w}_t \leftarrow \mathbf{w}_{t+1} + \mathbf{D}_z \hat{\mathbf{x}}'_t - \mathbf{z}_t$
 - 14: \triangleright DDIM sampling
 - 15: $\mathbf{x}_{t-1} \leftarrow \hat{\mathbf{x}}'_t - \sigma_{t-1}^2 \sqrt{1 - \eta^2} \hat{\mathbf{s}}_t + \sigma_{t-1} \epsilon$
 - 16: **end for**
 - 17: $\mathbf{x}_0 \leftarrow \mathbf{x}_1 + \sigma_1^2 s_{\theta^*}(\mathbf{x}_1)$
 - 18: **return** \mathbf{x}_0
-